



# 1 The Global SMOS Level 3 daily soil moisture and brightness 2 temperature maps

3 Ahmad Al Bitar<sup>1,2</sup>, Arnaud Mialon<sup>1,2</sup>, Yann H. Kerr<sup>1,3</sup>, François Cabot<sup>1,3</sup>, Philippe Richaume<sup>1</sup>,  
4 Elsa Jacquette<sup>3</sup>, Arnaud Quesney<sup>4</sup>, Ali Mahmoodi<sup>1</sup>, Stéphane Tarot<sup>5</sup>, Marie Parrens<sup>1</sup>, Amen Al-Yaari<sup>6</sup>,  
5 Thierry Pellarin<sup>7</sup>, Nemesio Rodriguez-Fernandez<sup>1</sup>, Jean-Pierre Wigneron<sup>6</sup>

6 <sup>1</sup> Centre d'Etudes Spatiales de la Biosphère, Université de Toulouse, CNES/CNRS/IRD/UPS, Toulouse,  
7 France.

8 <sup>2</sup> Centre National de Recherche Scientifique, Paris, France.

9 <sup>3</sup> Centre National d'Etudes Spatiales, Paris, France.

10 <sup>4</sup> CapGemini Sud, 109 Avenue du Général Eisenhower, 31000 Toulouse, France.

11 <sup>5</sup> IFremer, BP 70, 29280 Plouzane, France.

12 <sup>6</sup> INRA, UMR1391 ISPA, Villenave d'Ornon, France.

13 <sup>7</sup> IGE, University Grenoble Alpes, CNRS/G-INP/IRD/UGA, Grenoble, France.

14

15 *Correspondence to:* Ahmad Al Bitar (ahmad.albitar@cesbio.cnes.fr)

16 **Keywords:** soil moisture, SMOS, L-band, SMAP, Multi-orbit, microwave, retrieval algorithm

17 **Abstract:** The objective of this paper is to present the multi-orbit (MO) surface Soil Moisture (SM) and  
18 angle binned Brightness Temperature (TB) products for the SMOS (Soil Moisture and Ocean Salinity)  
19 mission based on the a new multi-orbit algorithm. The Level 3 algorithm at CATDS (Centre de Traitement  
20 Aval des Données SMOS) makes use of multi-orbit (multi-revisits) retrieval to enhance the robustness and  
21 quality of SM retrievals. The motivation of the approach is to make use of the temporal auto-correlation of  
22 the vegetation optical depth (VOD) to enhance the retrievals when an acquisition occurs at the border of  
23 the swath. The retrieval algorithm is implemented in a unique operational processor delivering multiple  
24 parameters (e.g. SM and VOD) using angular signatures, dual polarization and multiple revisits. A  
25 subsidiary angle binned TB product is provided. In this study the L3 TB V300 product is showcased and  
26 compared to SMAP (Soil Moisture Active Passive) TB. The L3 SM V300 product is compared to the  
27 single-orbit (SO) retrievals from Level 2 SM processor from ESA (European Space Agency) with aligned



28 configuration. The advantages and drawbacks of the Level 3 SM product (L3SM) product are discussed.  
29 The comparison is done at global scale between the two datasets and at local scale with respect to *in situ*  
30 data from AMMA-CATCH and USDA-ARS WATERSHEDS networks. The results obtained from the  
31 global analysis show that the MO implementation enhances the number of retrievals up to 9 % over  
32 certain areas. The comparison with the *in situ* data shows that the increase of the number of retrievals  
33 does not come with a decrease of quality. But rather at the expense of an increased lag of product  
34 availability from 6 hours to 3.5 days which can be a limiting factor for forecast applications like flood  
35 forecast but reasonable for drought monitoring and climate change studies. The SMOS L3 soil moisture  
36 and L3 brightness temperature products are delivered using an open licence and free of charge by CATDS  
37 (<http://www.catds.fr>).

### 38 **Abbreviations**

39	ARS	Agricultural Research Service
40	AMMA	Analyse Multidisciplinaire de la Mousson
41	AMSR-E	Advanced Microwave Scanning Radiometer - Earth Observing System
42	ASCAT	Advanced Scatterometer
43	CATDS	Centre Aval de Traitement des Données SMOS
44	CNES	Centre National d'Etudes Spatiales
45	CCI	Climate Change Initiative
46	CDTI	Centro para el Desarrollo Tecnológico Industrial
47	DPGS	Data Processing Ground Segment
48	EASE-Grid	Equal-Area Scalable Earth Grid
49	ECMWF	European Centre for Medium-Range Weather Forecasts
50	ECV	Essential Climate Variables
51	EO	Earth Observation
52	ESA	European Space Agency
53	IFREMER	Institut Français de Recherche pour l'Exploitation de la Mer
54	ISEA	Icosahedral Snyder Equal Area
55	L-MEB	L-band Microwave Emission of the Biosphere
56	MO	Multi Orbit
57	NASA	National Aeronautics and Space Administration (U.S.A.)
58	SM	Soil Moisture
59	SMAP	Soil Moisture Active and Passive



60	SMOS	Soil Moisture and Ocean Salinity
61	SMUDP	Soil Moisture User Data Product
62	SO	Single Orbit
63	TOA	Top of Atmosphere
64	USDA	United States Department of Agriculture
65	VOD	Vegetation Optical Depth



## 66 1. Introduction

67 Surface Soil Moisture (SM) is a control physical parameter for many hydrological processes like  
68 infiltration, runoff, precipitation and evaporation (Koster et al., 2004). Estimates of SM are needed for  
69 many applications concerned with monitoring droughts (Keyantash & Dracup, 2002), floods (Brocca et  
70 al., 2010, Lievens et al., 2015), weather forecast (Drusch, 2007, de Rosnay et al., 2013), climate (Jung et  
71 al. 2010), and agriculture (Guérif & Duke, 2000). It is identified among the 50 Essential Climate Variables  
72 (ECV) for the Global Climate Observing Systems (GCOS). It has been also selected for the creation of  
73 decadal time series from remote sensing in the European Space Agency (ESA) Climate Change Initiative  
74 (CCI) project (Hollmann et al., 2013).

75 SM can be obtained from several Earth Observation (EO) techniques ranging from visible to microwave  
76 using active (Ulaby et al., 1996) and passive (Kerr & Njoku. 1990) instruments. Retrieval of SM from  
77 microwave sensors is a challenging exercise because features like surface heterogeneity (water surfaces,  
78 land use), vegetation cover (vegetation density and distribution), climatic conditions (freezing, snow),  
79 acquisition configurations (angle, frequency, polarisation), and topography (multiple scattering) need to  
80 be carefully considered while upscaling to the sensor coarse resolution. Several approaches like regression  
81 models (Njoku et al., 2003, Wigneron et al., 2004 and Saleh et al., 2006), statistical and contextual  
82 methods (Verhoest et al., 1998), neural networks (Liu et al., 2002, Rodriguez-Fernandez et al., 2015) and  
83 radiative transfer based approaches (Kerr & Njoku, 1990, Wigneron et al., 2007, Owe et al., 2008, O'Neill  
84 et al., 2013) have been developed to retrieve SM based on the sensor frequency, acquisition modes and  
85 richness of information (multi angular, full polarization, active). The Soil Moisture and Ocean Salinity  
86 (SMOS) mission of ESA (Kerr et al., 2001, 2010) with contributions from Centre National d'Etudes  
87 Spatiales (CNES) in France and Centro para el Desarrollo Tecnológico Industrial (CDTI) in Spain is the  
88 first earth observation mission dedicated for SM mapping. The SMOS Level 2 (L2) SM retrieval  
89 algorithm (Kerr et al., 2012) uses the L-band Microwave Emission of the Biosphere (L-MEB) radiative  
90 transfer model (Wigneron et al., 2007) as a forward operator in association with the Levenberg-Marquardt  
91 optimization algorithm to retrieve physical parameters, mainly SM and VOD.



92 The L-MEB radiative transfer model is based on the optical depth single scattering albedo ( $\tau-\omega$ ) model  
93 (Mo et al., 1982) combined to specific parameterisations to take into account the impact of vegetation and  
94 soil roughness on polarization mixing and angular signature. The Soil Moisture Active Passive (SMAP)  
95 mission, launched by NASA on January 2015 delivers TB observations on a fixed ( $40^\circ$ ) incidence angle  
96 (Entekhabi et al. 2010). The SMAP soil moisture processor currently relies on a Single Channel Algorithm  
97 (SCA) (O'Neill et al., 2012) for its main product. This algorithm uses a forced vegetation optical thickness  
98 in a single-orbit configuration. Miernecki et al. (2015) presented a review and a comparison of the  
99 different retrieval approaches for L-Band microwave from EO missions (SMOS, SMAP, AQUARIUS).

100 Passive microwave sensors have a high revisit frequency: 1 day for Advanced Microwave Scanning  
101 Radiometer - Earth Observing System (AMSR-E) (Njoku & Entekhabi, 1996), and 2-3 days for SMOS  
102 and SMAP. In this study the multiple orbit (MO), multi-angular and dual channel (H/V) operational  
103 retrieval algorithm implemented at the CATDS (Centre Aval de Traitement des Données SMOS) by  
104 Centre National d'Etudes Spatiales (CNES) is presented. Retrieval using temporal series is becoming  
105 increasingly common in operational EO retrieval algorithms for optical and to some extent microwave  
106 technologies. Some examples in the optical domain are the correction of aerosols impact for visible  
107 images (Hagolle et al., 2008, 2015), the cloud detection (Hagolle et al., 2010) and the use of multiple  
108 revisits for land cover classification (Inglada & Mercier, 2007). The previous methodologies are being  
109 implemented for high-end level 2-A and level 3 products for the Copernicus Sentinel-2 mission. The use  
110 of multiple revisits in the radar community is a standard approach. The SM retrievals from ERS,  
111 Advanced Scatterometer (ASCAT), RADARSAT-2 and Sentinel-1 are based on a change detection  
112 algorithm (Wagner et al., 1999, 2013; Naeimi et al., 2009). Similarly, Mattia et al. (2006) introduced a  
113 priori surface parameters and multi-temporal Synthetic Aperture Radar (SAR) data to remove the impact  
114 of vegetation and soil roughness in SM retrieval from SAR. Recently a generalization of change detection  
115 to multiple regression using Cumulative Distribution Function (CDF) transformations was applied to  
116 RADARSAT-2 time series data and validated over the Berambadi watershed, South India (Tomer et al.,  
117 2015). In microwave radiometry, Konings et al. (2016) presented a time series retrieval of vegetation  
118 optical depth based on AQUARIUS L-Band acquisitions.



119 Here a detailed presentation of the products and retrieval algorithm and an inter-comparison between the  
120 SMOS SO (Single orbit) and the SMOS MO (Multi-orbit) operational products is done. More  
121 specifically, the objective of this paper is to present the daily L3 SM and TB V300 products and  
122 associated algorithms and to compare the SMOS MO level 3 retrievals to the level 2 single-orbit  
123 operational retrievals that are were obtained using V600 L1 ESA-SMOS products. Since the SMOS  
124 mission launch in November 2009, this is the first reprocessing to have an aligned version of the  
125 processors from Level 1 up to Level 3 enabling a direct comparison of the products. In the next sections,  
126 the multi-orbit retrieval SM algorithm and the angle binned TB are presented. The datasets used for the  
127 assessment, the results of the comparison and conclusions are presented.

## 128 **2. The CATDS Level-3 soil moisture processor**

### 129 **2.1 Algorithm overview**

130 The Level-3 SM (L3SM) processor is a set of several algorithms. The forward model in L3SM uses the  
131 same physically based forward models as the ESA SMOS Level 2 SM processor, but in a MO retrieval  
132 context. A short summary of the main features of this processor is provided hereby, a detailed description  
133 is provided in (Kerr et al. 2012). The SMOS L2 retrieval can be divided into two main components:

134 1) The first component is a physical model that computes TB at the antenna reference frame forced by  
135 ancillary data (land classification, soil properties) and physical parameters (skin or near-surface  
136 temperature and soil temperature).. The selected physical model for the SMOS mission is L-MEB from  
137 Wigneron et al. (2007). The main features of the L-MEB physical model implementation in the SMOS  
138 operational processor are:

- 139 • Effective scattering albedo is considered.
- 140 • SM and VOD are jointly retrieved over nominal (bare soil and low vegetation) surfaces using  
141 angular signature information.
- 142 • Dual polarization is used. Full polarisation data is only used to take into account the Faraday  
143 rotation and geometric rotation to transform modelled TB from the Top Of Atmosphere (TOA) to  
144 the antenna reference frame.



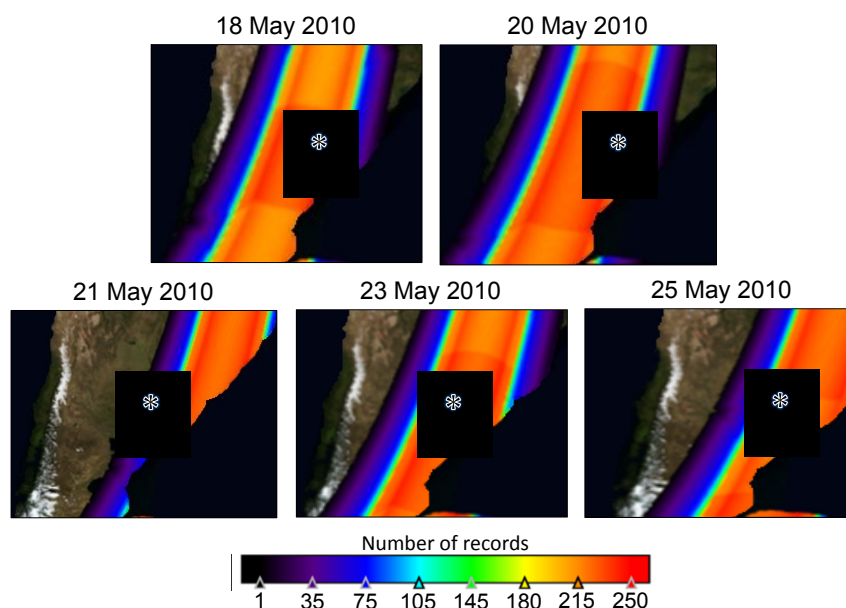
- 145       • The mean antenna pattern (Kerr et al., 2012) is used in the iterative retrieval algorithm. The mean  
146       weighting function expresses the average contributions for all angular acquisitions. The -3 dB  
147       footprints is about 20 km in radius. This corresponds to the nominal resolution of the synthetic  
148       aperture. Also this corresponds to 86% of the signal if a homogeneous surface is considered (Al  
149       Bitar et al., 2012).
- 150       • Surface heterogeneity is considered through aggregated TB contributions from  $4 \times 4$  km<sup>2</sup> surface  
151       units. The contributions are then convoluted by the mean antenna pattern. A total area of  $125 \times$   
152       125 km<sup>2</sup> is considered at each retrieval node to compute the total contributions.
- 153       • Dynamic changes in surface state (freezing, rainfall...) are considered through the use of ancillary  
154       weather data from ECMWF (European Centre for Medium-Range Weather Forecasts) reanalysis  
155       products.

156       Since the mission launch many improvements have been implemented in the operational processing  
157       model see for instance the improved parametrization of the forest albedo in Rahmoune et al., (2014) or  
158       the choice of dielectric mixing models in Mialon et al., (2015).

159       2) The second component of the retrieval algorithm is an iterative optimization scheme that minimises a  
160       Bayesian cost function constructed from the observed and the modelled TBs in order to retrieve the  
161       physical parameter values. Pre-processing and post-processing steps are implemented to filter the input  
162       and output data for undesired effects, like the decrease of quality due to spatial sampling or Radio  
163       Frequency Interferences (RFI) (Oliva et al., 2012, Richaume et al., 2014).

164       The physical approach at Level-3 MO is the same as that of Level-2 SO. In fact the core processing uses  
165       the same implementation of the L-MEB radiative transfer model. The main difference in Level-3 is the use  
166       of several orbits, rather than one, to retrieve SM and VOD. This has an impact first on the post-processing  
167       steps for selecting the orbits and second on the optimization scheme to retrieve the parameters. Since the  
168       Level-2 retrieval is a multi-parameter retrieval, the Level-3 is thus a multi-orbit multi-parameter retrieval.  
169       The reasons that motivated the use of the MO approach are the following:

170 • The angular sampling and radiometric accuracy at the border of the swath is reduced. Figure 1  
171 shows the cumulative number of records ( $TB_x$ ,  $TB_y$ ,  $TB_{xy}$ ) for several descending orbits. The  
172 asterisk in the images represents the same location in La Plata region, South-America. The reddish  
173 region observed on 18<sup>th</sup>, 20<sup>th</sup> and 23<sup>rd</sup> of May 2010 shows the decrease of number of TB  
174 measurements during the instrument calibration phases. But most important is the smaller number  
175 of TB measurements (35) on the same location observed on the 21<sup>th</sup> of May image. A low  
176 number of TB measurements spanning a narrow range of incidence angles can make the iterative  
177 estimation of SM and VOD to fail. The use of MO can help improving the number of successful  
178 retrievals at the border.



179

180 *Figure 1 - Number of TB records across the swath for a period of 8 days - from 18 May*

181 *2010 to 25 May 2010 - over the area of La Plata Argentina.*

182 • The VOD is expected to vary slowly in time and thus to be highly correlated between two  
183 consecutive ascending or descending orbits or over short period of time (few days). In fact at L-  
184 band the VOD is mainly correlated to vegetation water content (Jackson & Schmugge, 1991).





185 Other general motivations for Level-3 products are to provide a global gridded product, in contrast to  
186 swath based products and to provide fixed angle binned TB products. The 25 km Equal-Area Scalable  
187 Earth Grid version 2.0 (EASE-Grid 2.0) (Brodzik & Knowles, 2002) which was selected for the 3 MO  
188 product has also a spatial sampling closer to the sensor nominal resolution.

## 189 **2.2 Orbit selection**

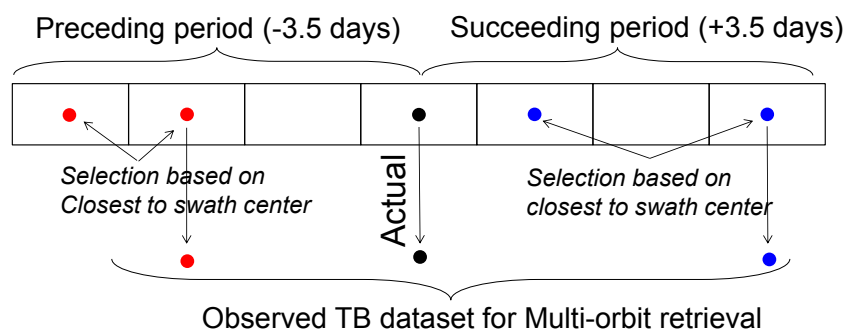
190 The selection of orbits is needed to filter TBs at high latitudes where a sub-daily revisit is available and to  
191 generate the time series dataset on the EASE-Grid 2.0 as input to the MO retrieval. The following criteria  
192 are applied for the selection of revisits:

- 193 • Ascending and descending orbits are processed separately, since the impact of RFI (Oliva et al.,  
194 2012) and sun corrections (Khazaal et al., 2016) between ascending and descending orbits are  
195 very different.
- 196 • TB products are generated from the snapshot based L1B products which are TBs in the Fourier  
197 domain. This consists in an Inverse Fast Fourier Transform (IFFT) to make the transition from the  
198 Fourier domain to the spatial domain using the L3 EASE-Grid 2.0. In a subsequent step, TBs  
199 measurements corresponding to the same grid point are selected from the different snapshots (for  
200 a given grid point, the incidence angle of the observation is different for each snapshot) to  
201 construct a grid-point-based product similar to the ESA L1C TB product but in EASEv2 grid. The  
202 alternative of interpolating the ESA L1C TB dataset from the 15 km Icosahedral Snyder Equal  
203 Area (ISEA) grid to the 25km EASE-Grid 2.0 grid. This option was excluded because it can  
204 generate interpolation artefacts on the TB products that would have propagated through the  
205 processing chain.
- 206 • TB products are filtered at high latitudes where more than one revisit per day occurs (latitudes  
207 above 60°N and 60°S). A maximum of one revisit per day is considered. The selection criterion is  
208 the minimum distance from the centre of the swath because the radiometric accuracy and  
209 resolution is best at the centre. This criterion is applied for each grid node individually.



210 At this level the acquisitions for a given day for ascending and descending orbits are separately stored in a  
211 3 dimensional matrix accounting for snapshots, longitude and latitude. A snapshot is an image associated  
212 to the acquisition of SMOS during a given integration time (epoch). Snapshots have different epochs and  
213 polarization following a preprogramed acquisition sequence. From this product a fixed angle binned TB  
214 product is generated as presented in Section 3. The product is also used in the next processing steps of  
215 L3SM MO.

- 216 • For each retrieval and over each node a 7-days period is considered in which 3 revisits are  
217 selected when more are available. The first coincides with the central date (date of main product).  
218 The two others correspond to selected dates either before (previous 3.5 days) or after (3.5 days  
219 posterior) the considered date. Like in the previous processing step, the selection is done based on  
220 minimum distance from the swath centre for each node.



221

222

Figure 2 - Selection of revisit orbits for the multi-orbit retrieval at SMOS CATDS.

### 223 2.3 Cost function and retrieval

224 Observed TB at antenna reference frame from the “precedent”, “actual” and “succeeding” dates are  
225 assembled for each node. The forward algorithm is run to generate the modelled TB for each of the TB  
226 dataset records. The ancillary data and parameters are considered for each record independently. A  
227 Bayesian cost function that includes the aforementioned MO data, namely observed and modelled TB, is  
228 then constructed. This is achieved by incorporating in the retrieval approach a temporal auto-correlation  
229 function for the VOD. The cost function is as follows:



$$230 \quad Cost = (TB_M - TB_F)^t \cdot \mathbf{COV}_{TB}^{-1} \cdot (TB_M - TB_F) + \sum_p (P - P_0)^t \cdot \mathbf{COV}_p^{-1} \cdot (P - P_0) \quad (1)$$

231 Where  $\mathbf{COV}_{TB} = \sigma_{TB}^2$  is the error covariance matrix of TB data by assuming no auto-temporal correlation,  
 232  $TB_M$  is the measured TB from SMOS,  $TB_F$  is the forward modelled TB using L-MEB,  $P$  is the retrieved  
 233 parameters (SM, VOD),  $\mathbf{COV}_p$  is the error covariance matrix for parameter  $P$ .  $P_0$  is the a-priori value of  
 234 parameter  $P$ .

235 It is important to note that three SM values are retrieved simultaneously at each node:  $SM_p$  for the  
 236 preceding date,  $SM_A$  for the actual date and  $SM_F$  for the succeeding date. The same applies to VOD. In the  
 237 case of SM, the a-priori values are given from ECMWF reanalysis data.

238 When  $P = SM_p, SM_A$  or  $SM_F$ , the error covariance matrix considering no-cross or auto-correlation is given  
 239 by:

$$240 \quad \mathbf{COV}_{SM} = \sigma_{SM0}^2 \cdot \mathbf{I} \quad (2)$$

241 where  $\sigma_{SM0}^2$  is the standard-deviation error associated to SM. It is set to a high value:  $0.7 \text{ m}^3/\text{m}^3$ .  $\mathbf{I}$  is the  
 242  $(3 \times 3)$  identity matrix.

243 When  $P = \text{VOD}$  the error covariance matrix, considering temporal auto-correlation and no-cross  
 244 correlation between the different parameters is given by:

$$245 \quad \mathbf{COV}_{VOD} = \sigma_{VOD0}^2 \begin{bmatrix} 1 & \dots & \dots \\ \rho(t_p, t_A) & 1 & \dots \\ \rho(t_p, t_F) & \rho(t_A, t_F) & 1 \end{bmatrix} \quad (3)$$

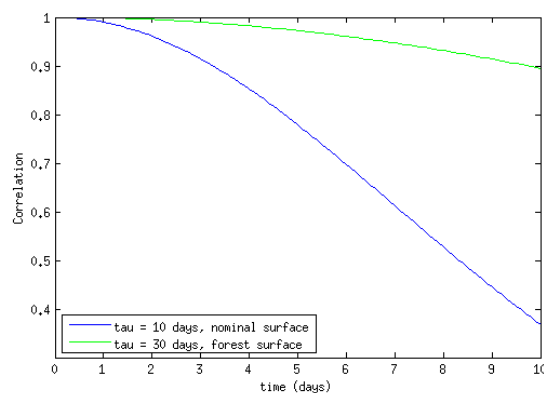
246 Where  $\sigma_{VOD0}^2$  is the standard-deviation error associated to VOD, and  $\rho$  the correlation function modelled  
 247 assuming a Gaussian auto-correlation distribution:

$$248 \quad \rho_{VOD}(t_1, t_2) = \rho_{max}(t_1, t_2) \cdot \exp\left(-\frac{(t_1 - t_2)^2}{Tc^2}\right) \quad (4)$$

249 Where  $t_1$  and  $t_2$  are the time (expressed in days) corresponding to the VOD retrievals dates (P, A or F),  
 250  $\rho_{max}(t_1, t_2)$  is the maximum amplitude of the correlation function between  $t_1$  and  $t_2$ ,  $Tc$  is the characteristic  
 251 correlation time for VOD ( $Tc = 30$  days for forests and  $Tc = 10$  days for low vegetation).



252 Figure 3 shows the shape of the correlation function for the two correlation lengths used in the processing.  
253 The green curve corresponds to the forested surfaces and the blue one to the nominal surfaces (bare soil  
254 and low vegetation).



255

256 *Figure 3 Auto-correlation functions for vegetation optical depth (VOD) for different*  
257 *correlation lengths (green: forested surfaces, blue: nominal surfaces).*

258 The parameter values namely ( $SM_P$ ,  $SM_A$ ,  $SM_F$ ,  $VOD_P$ ,  $VOD_A$  and  $VOD_F$ ) are retrieved by minimising the  
259 cost function in an iterative procedure using the Levenberg-Marquardt optimisation algorithm. So, at the  
260 end of each daily retrieval, three SM values are available. The retrieval associated to the best goodness of  
261 fit ( $X^2$ ) value is then selected and delivered in the 1 day product. This product is only available when the  
262 filtering is finished, and thus with 7 days of lag time. Using the daily maps, time synthesis products (3  
263 days, 10 days and monthly) are then provided. A detailed description of the algorithm is presented in the  
264 CATDS L3 Algorithm Theoretical Basis Document (Kerr et al.,2013).

### 265 3. The CATDS Level-3 angle binned TB processor

266 The objective of this algorithm is to generate a product containing fixed angle full polarization brightness  
267 temperatures at Top of Atmosphere (TOA) but with the polarizations expressed in the ground reference  
268 frame (horizontal and vertical components) over the EASE-Grid 2.0. The main input to this algorithm is  
269 the dataset of snapshots mentioned in the previous section. The algorithm consists of four steps: (a)  
270 filtering, (b) interpolation, (c) reference transformation and (d) angle binning. However note that before  
271 being projected to a ground frame, the data is processed in the instrument reference frame. Thus TBs are



272 labelled  $TB_Y$  and  $TB_X$  to express that the polarisations are at satellite level while once processed they will  
 273 be provided in the ground reference frame and be labelled  $TB_H$  and  $TB_V$ .

274

### 275 3.1 TB filtering

276 The filtering eliminates brightness temperatures that are impacted by anthropogenic effects (such as Radio  
 277 Frequency Interferences (RFI)), or spurious effects (such as sun impact). The filtering criteria, shown in  
 278 Table 1, are similar to those for L3 MO SM retrieval. All filtering criteria should be met, otherwise the  
 279 acquisition is discarded. In case a cross-polarisation is discarded, the associated X and Y acquisitions are  
 280 also removed.

Table 1 – List of applied filtering criterion used on brightness temperature products prior to interpolation

Filtering criteria	Applied test	Filtering criteria	Applied test
thresholds	$50 \text{ K} < TB_X \text{ \& } TB_Y < 340 \text{ K}$	RFI	L1A STRONG RFI (flag is off)
	$-50 \text{ K} < TB_{xy} < +50 \text{ K}$		L1B STRONG RFI (flag is off)
Amplitude	$50 \text{ K} < \sqrt{TB_X^2 + TB_Y^2} < 500 \text{ K}$		POINT SOURCE RFI (flag is off)
Standard deviation	$TB - 2 \cdot ATB < TB < TB + 2 \cdot ATB$		TAILS RFI (flag is off)
1 <sup>st</sup> Stokes	$ST1 - \overline{ST1} < 5 + 4 \cdot ATB$		
Spatial resolution †	$SMEF < (55 \times 55) \text{ km}^2$	Sun correction ‡	SUN_POINT (flag is off)
	$LMA / Lmi < 1.5$		SUN_TAILS (flag is off)
	BORDER FOV (flag is off)		

281 Where  $ATB$  is the radiometric accuracy of SMOS  $TB$ ,  $ST1$  is the first Stokes parameter,  $\overline{ST1}$  is the average of  $ST1$  over each dwell  
 282 line (angular signature),  $ST4$  is the forth Stokes parameter,  $SMEF$  is the area of the half maximum contour of the mean synthetic  
 283 antenna pattern,  $LMA$  Length of the major axis of synthetic antenna pattern,  $Lmi$  Length of the minor axis of synthetic antenna  
 284 pattern.

285 † Spatial resolution: eliminates records that are impacted by aliasing (outside the alias free field of view).

286 ‡ if active the flag means that the pixel is located in a zone where a Sun alias was reconstructed (after sun removal, measurement  
 287 may be degraded). The sun tail is considered when the pixel is located in the hexagonal alias directions centred on a sun alias.

### 288 3.2 TB Interpolation

289 The acquisition sequence of SMOS is shown in Table 2. It shows that at each epoch an acquisition can be  
 290 co-polarised (X, Y) or combined cross (XY, YX) and co-polarised. The table shows that there is no



291 complete dataset at any epoch. A weighted linear interpolation is used to compute the missing acquisitions  
 292 based on adjacent ones.

Table 2 - Acquisition sequences of SMOS in full polarization mode (capital letters are used for pure acquisition)

Snapshot number	1	2	3	4	5	6	7	8	9	10	11	12
TB (Real/Imaginary)		X/XY		Y/YX		X/XY						Y/YX
TB (co-polarisation)	X	X	Y	y	X	x		Y	X		Y	Y

293  
 294 The weighting function accounts for the two following elements:  
 295 - The accuracy of acquisition: the TB acquisitions have different accuracy levels because the integration  
 296 time is longer when only co-polarisation is acquired (pure acquisition) compared to the case where  
 297 combined cross and co-polarisation are acquired.  
 298 - The time span of acquisition: The time span between two acquisitions of the same mode is not constant.  
 299 Acquisitions closer in time are considered more reliable than farther ones taking into consideration that the  
 300 synthetic antenna function is rotating and that the incidence angle is changing.  
 301 The time interpolation function of TB at time  $i$  ( $TB_i$ ) is as follows:

$$\left\{ \begin{array}{l} TB_i = \frac{W_{i-1} \cdot TB_{i-1} + W_{i+1} \cdot TB_{i+1}}{W_{i-1} + W_{i+1}} \\ W_{i-1} = \frac{1}{\sigma_{i-1} \cdot nb\_epo_{i-1}} \\ W_{i+1} = \frac{1}{\sigma_{i+1} \cdot nb\_epo_{i+1}} \end{array} \right. \quad (5)$$

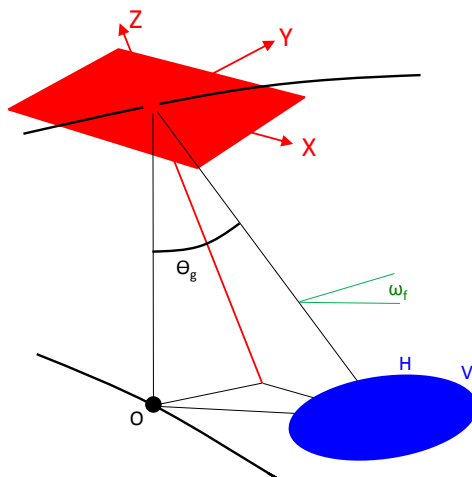
302  
 303 Where  $nb\_epo_i$  is the number of epochs between acquisitions at time  $i$ ,  $\sigma$  is the associated radiometric  
 304 accuracy,  $W_i$  is the weighting coefficient at time  $i$ . The standard deviation of the interpolated field is  
 305 computed based on the square root of the weighted variances of the adjacent acquisition. We assume that  
 306 the acquisitions are not-correlated, therefore no cross correlation term is considered in the equation. The  
 307 following formulation is used:

$$\left\{ \begin{array}{l} \sigma_i = \sqrt{\frac{(Q_{i-1} \cdot \sigma_{i-1})^2 + (Q_{i+1} \cdot \sigma_{i+1})^2}{Q_{i-1}^2 + Q_{i+1}^2}} \\ Q_i = \frac{1}{nb\_epo_i} \end{array} \right. \quad (6)$$

308 The same approach as eq.(5) while applying a constant weight is used to compute the interpolated values  
 309 of auxiliary information like major and minor semi-axis length, incidence angle, Faraday angle and  
 310 geometric angle.

### 311 3.3 Transformation from antenna to ground reference frame

312 In this step, the TBs are transformed from antenna reference frame (X,Y) to the ground reference frame  
 313 (H,V). This is done without accounting for atmospheric and galactic contributions. They are considered as  
 314 TOA TBs. The TB components at antenna reference frame exhibit polarisation mixing due to the geometry  
 315 of the acquisition (Figure 4). Faraday rotation will also alter slightly the polarisations.



316

Figure 4 - Transformation from antenna (S) to ground reference frame (G),  $\omega_f$  is the faraday rotation angle and  $\theta_g$  is the geometric rotation angle (adapted from SMOS L2 ATBD).

317 The inverse of the rotation matrix is used to transform the TB data from antenna to ground reference  
 318 frame:

$$319 \begin{bmatrix} TB_H \\ TB_V \\ TB_3 \\ TB_4 \end{bmatrix} = IRM \begin{bmatrix} TB_X \\ TB_Y \\ 2 \cdot \text{reel}(TB_{XY}) \\ -2 \cdot \text{imag}(TB_{XY}) \end{bmatrix} \quad (7)$$

320  $TB_3$  and  $TB_4$  are the Stokes 3 and Stokes 4 components. The Inverse of Rotation Matrix (IRM) is given by:  
 321

$$322 IRM = \begin{bmatrix} \cos^2 a & \sin^2 a & \cos a \cdot \sin a & 0 \\ \sin^2 a & \cos^2 a & -\cos a \cdot \sin a & 0 \\ -\sin 2a & \sin 2a & \cos 2a & 0 \\ 0 & 0 & 0 & 1 \end{bmatrix} \quad (8)$$



323 Where  $a = \theta_g + \omega_f$  (9)  
 324 With  $\theta_g$  being the geometric angle and  $\omega_f$  being the Faraday rotation angle as shown in Figure 4.

325  
 326  
 327

328 The accuracies of the TB data are then computed by propagating the accuracies using the above matrix:

$$329 \begin{cases} \sigma_{TBH} = (IRM_{1,1}^2 \cdot \sigma_{TB_X}^2 + IRM_{1,2}^2 \cdot \sigma_{dTB_Y}^2 + 4 \cdot (IRM_{1,3}^2 + IRM_{1,4}^2) \cdot \sigma_{TB_{XY}}^2)^{0.5} \\ \sigma_{TBV} = (IRM_{2,1}^2 \cdot \sigma_{TB_X}^2 + IRM_{2,2}^2 \cdot \sigma_{dTB_Y}^2 + 4 \cdot (IRM_{2,3}^2 + IRM_{2,4}^2) \cdot \sigma_{TB_{XY}}^2)^{0.5} \\ \sigma_{TB3} = (IRM_{3,1}^2 \cdot \sigma_{TB_X}^2 + IRM_{3,2}^2 \cdot \sigma_{dTB_Y}^2 + 4 \cdot (IRM_{3,3}^2 + IRM_{3,4}^2) \cdot \sigma_{TB_{XY}}^2)^{0.5} \\ \sigma_{TB4} = (IRM_{4,1}^2 \cdot \sigma_{TB_X}^2 + IRM_{4,2}^2 \cdot \sigma_{dTB_Y}^2 + 4 \cdot (IRM_{4,3}^2 + IRM_{4,4}^2) \cdot \sigma_{TB_{XY}}^2)^{0.5} \end{cases} \quad (10)$$

330 Where  $IRM_{i,j}$  are the  $i^{\text{th}}$  column and  $j^{\text{th}}$  line components of the IRM matrix

### 331 3.4 Angle binning

332 This step consists of averaging the TOA TBs at fixed angle intervals using an arithmetic mean. The  
 333 selected incidence angle bins, shown in Table 3, are designed to cover also the SMAP acquisition angle  
 334 ( $40^\circ$ ).

Table 3 - Selected incident angle bins

Bin id	1	2	3	5	6	7	8	9	10	11	12	13	14
Bin centre	2.5°	7.5°	17.5°	22.5°	27.5°	32.5°	37.5°	40°	42.5°	47.5°	52.5°	57.5°	62.5°
Bin width	5°	5°	5°	5°	5°	5°	5°	5°	5°	5°	5°	5°	5°

335

336 All TB values outside the interval defined by  $\text{mean (TB)} \pm 2 \text{ std (TB)}$ , where is the standard deviation of  
 337 TB for each angle bin (not to be confused with the radiometric accuracy), are considered as outliers and  
 338 removed from the binning. This helps the removal of the low RFI effects and other undesired impacts. If  
 339 one component of TB ( $TB_H, TB_V, TB_{HV}$ ) is filtered out, all the other components are disregarded.

340





341 **4. Datasets**

342 **4.1 Remote sensing datasets**

343 **4.1.1 SMOS CATDS Level 3 soil moisture products**

344 The CATDS Level 3 user data products (CLF3UA/D) are MO soil moisture retrieval products. They  
345 contain 1 day global maps of geophysical parameters (SM, VOD, imaginary and real dielectric constant  
346 part...) computed as described above, processing parameters (percentage of forest cover, type of surface  
347 model...) and quality indicators (Probability of RFI, goodness of fit  $X^2$  ...) over continental surfaces for  
348 ascending and descending orbits separately. They are in the NetCDF format over the EASE-Grid 2.0 25  
349 km. They are generated at the Institut Français de Recherche pour l'Exploitation de la Mer (IFREMER)  
350 for CNES and distributed via the CATDS webportal (<http://www.catds.fr>) and ftp server. The operational  
351 production of L3SM started in 2010 and it is currently ongoing. The time span used in this study covers  
352 2010 - 2015 for the global maps and 2010 - 2016 for the time series analysis. The user has access to the  
353 latest versions of the products either from reprocessing or from operational processing. The current study  
354 uses the latest data corresponding to reprocessing RE04 which uses CATDS V300 corresponding to ESA  
355 V620 Level 1 & 2. It is the first simultaneous Level 2 and Level 3 reprocessing campaign since the start of  
356 the mission. Previous versions of the L3SM products were compared to soil moisture products from  
357 AMSR-E (Al-Yaari et al., 2014 a) and ASCAT (Al-Yaari et al., 2014 b) missions, but this is the first  
358 comparison enabling a aligned configuration of the L2SM SO and L3SM MO. It has homogenized inputs  
359 (L1B/C) and physical parametrization. It uses the Mironov dielectric constant model (Mialon et al., 2015),  
360 enhanced forest parametrization for albedo (Rahmoune et al., 2014), enhanced global soil texture map  
361 consistent with the one used for the SMAP mission, and latest RFI detection techniques (Richaume et al.,  
362 2014). It uses also the latest (V620) brightness temperature products at Level 1B. The SM maps are  
363 extracted in the present study from the L3 product. After extraction, RFI filtering is applied with  
364 Probability of RFI < 10 % and goodness of fit with a probability of  $X^2 > 0.95$ .

365



#### 366 4.1.2 SMOS DPGS Level 2 soil moisture product

367 The ESA L2 Soil Moisture User Data Product (SMUDP), which is a SO retrieval product, is used in this  
368 study for comparison purposes. This product is a half-orbit swath based dataset of physical variables (SM,  
369 VOD, dielectric constant imaginary and real part...), processing parameters (percentage of forest cover,  
370 type of surface model...) and quality indicators (Probability of RFI,  $X^2$ , ...) over continental surfaces.  
371 Ascending and descending orbits are processed separately in the current configuration. The SMUDP  
372 product is delivered in the BinX format over the ISEA discrete global grid (Carr et al. 1997), with a  
373 hexagonal partitioning of aperture 4 at a resolution of 9 km known as ISEA4H9. The grid point centres  
374 have a fixed separation distance of around 15 km. Products are generated at the ESA SMOS Data  
375 Processing Ground Segment (DPGS) and disseminated by ESA via Earth Online. The DPGS and CATDS  
376 share the same reprocessing dissemination strategy, and users are provided access to the most recent  
377 products even before the end of reprocessing campaign. Version 620 of SMUDP is used in this study, and  
378 the time span selected is 2010-2015 for the global analysis and 2010 – 2016 in the time series analysis.

379 The main characteristics and differences between the L2SM SO retrieval and L3SM MO retrieval  
380 products are summarised in Table 4.

#### 381 4.1.3 SMOS CATDS Level 3 brightness temperature products

382 The SMOS CATDS full polarisation angle binned daily brightness temperature product (CDF3TA/D)  
383 version 310 were downloaded from the same database as the L3 MO SM. These products consist of global  
384 1 day maps of full polarisation TB over fixed angle bins with their associated accuracies. Detailed  
385 computation was described above in Section 3. The product also contains auxiliary data like the geometric  
386 angles, Faraday angles, length of major semi-axis and length of minor semi-axis. Quality flags are also  
387 provided in the product. The  $TB_H$  and  $TB_V$  records are extracted for the  $40^\circ$  bin. No additional filtering is  
388 done over these products.

#### 389 4.1.4 SMAP NSIDC L1C brightness temperature

390 The SMAP mission from NASA was launched in January 2015. It operates like SMOS in L-band using a  
391 radiometer and a radar (that was operational for about 80 days). It has a local overpass time at 6H00 am



392 and 6H00 pm for ascending and descending orbits respectively but the acquisitions are not necessarily  
 393 synchronous with SMOS. In this study we use the SMAP TB derived from the radiometer acquisitions.  
 394 The SMAP L3B\_SM\_P product is downloaded from the National Snow and Ice Data Centre (NSIDC)  
 395 website. The SMAP L3 TB is used as input for the SM retrievals and it is corrected for the water  
 396 contribution and atmospheric effects. It is provided on the EASE 2.0 grid with a 36 km resolution product.  
 397 The data is in HDF5 format. The  $TB_H$  and  $TB_V$  records are extracted for year 2015.

Table 4 – Main characteristics of the SMOS Level 3 and Level 2 SM products

Product	L3SM	L2SM
Name of product	MIR_CLF3A/D	MIR_SMUDP
Gridding system	EASEv2	ISEA 4H9
Product sampling	25 km at	15 km fixed
Resolution	<i>SMOS nominal resolution of 40km</i>	
Multi-parameter retrieval	yes	Yes
Angular signature	yes	Yes
Polarization impact	yes	Yes
Multi-orbit	yes	No
Forward model	<i>L-MEB (tau omega)</i>	
Availability	3.5 - 7 days	6 hours
Processing centre	CATDS (CNES)	DPGS (ESA)
Format	NetCDF	BinX
Version	V300	V620
Coverage	Global grid	Swath based

398

#### 399 4.2 *In situ* datasets

400 In this study, the SMOS soil moisture products are evaluated against two networks with spatially  
 401 distributed soil moisture data at the footprint scale (USDA Watersheds and AMMA CATCH). The *in situ*  
 402 soil moisture data from probes installed at near surface are used. These sites provide a soil moisture  
 403 reading, representative of the first 5 cm of the top soil layer, as they are vertically installed. This may lead  
 404 to a mismatch between the sensor sampling depth and the expected representative depth 0-2 cm or 0-3 cm  
 405 of the L-Band microwave radiometers (Escorihuela et al., 2010). The choice of the sites is done to cover



406 contrasting environments over two different continents to provide an overview of the SM MO processor  
407 performances. The statistics over the sites are computed for data available within 1 hour of space-borne  
408 acquisitions (SMOS, SMAP).

#### 409 **4.2.1- AMMA dataset**

410 The AMMA long term observing system (AMMA-CATCH (1996) and AMMA-CATCH (2005)) includes  
411 three mesoscale sites located in Niger, Benin, and Mali that are representative of the West-African eco-  
412 climatic gradient (Cappelaere et al., 2009; Mougin et al., 2009).. The AMMA-CATCH soil moisture  
413 network is a well-established network in terms of satellite product assessment (de Rosnay et al., 2009;  
414 Pellarin et al., 2009; Louvet et al., 2015). Niger and Benin, of the three meso-scale sites, are selected for  
415 this study. The Niger site, centred at 13.645° N–2.632° E, is mainly composed of tiger bush on the  
416 plateaus, fallow savannah and pearl millet crop fields on the sandy slopes (Cappelaere et al., 2009). The  
417 Benin site, located at 1.5–2.8° E; 9–10.2° N, is mainly composed of Woody savannah and tropical forest.  
418 Most of ground-based instruments are located in the North–West part of the Ouémé catchment (9.745° N–  
419 1.653° E). The observed annual rainfall amount was 1578 mm in 2010, 1093 mm in 2011 and 1512 mm in  
420 2012.

#### 421 **4.2.2- USDA - WATERSHEDS**

422 The United States Department of Agriculture (USDA) Agricultural Research Service operates a network  
423 of densely instrument watershed across the US. Surface soil moisture (5 cm) is monitored across the  
424 watersheds and recorded on an hourly basis since 2002. The USDA provides estimates of the average soil  
425 moisture over an area that has approximately the size of a SMOS footprint. Two of the watersheds have  
426 been selected for this study: Walnut Gulch (WG), Arizona, USA (Keefer et al., 2008) and Little Washita  
427 (LW), Oklahoma, USA (Elliott et al., 1993). Soils in WG can be classified as sandy loam. The original  
428 datasets are available from <https://www.tucson.ars.ag.gov/dap/> for WG and from  
429 <http://ars.mesonet.org/webrequest/> for LW. Over LW the soil properties are more heterogeneous with a  
430 loam, clay and sand texture. Previous studies on calibration and scaling have quantified the uncertainty of  
431 the *in situ* measurements over the sites to be lower than 0.01 m<sup>3</sup>/m<sup>3</sup> when compared to gravimetric



432 measurements. The basin scale weighted average is based on the Thiessen polygon method and has a  
 433 standard deviations between 0.05 and 0.10 m<sup>3</sup>/m<sup>3</sup>. A detailed description of the site characteristics is  
 434 provided in Jackson et al. (2010), and details on the averaging procedure are provided in Jackson et al.  
 435 (2012). This network has been used for validation of remote sensing soil moisture datasets (including  
 436 SMOS) in many studies (Sahoo et al. 2008, Jackson et al. 2012, Leroux et al. 2014). Information on land  
 437 use and topography of these sites is provided in Table 5.

*Table 5 – Properties of the in situ sites used for the evaluation*

Network (number of stations)	Location	Vegetation/climate	Soil texture	Topography
<b>Walnut Gulch Watershed</b>	Southeastern Arizona, USA	Brush- and grass-covered-Desert shrubs rangeland-Cattle grazing/ Semiarid	Range/sandy loam	Rolling
<b>Little Washita watershed</b>	Southwest Oklahoma, USA	Rangeland and pasture (63%), winter wheat / Sub humid	Range-wheat/silt or sand	Rolling
<b>AMMA Catch network Niger</b>	Niger	South Sahelian climate with semi-arid vegetation and crops (millet, fallows and tiger bush).	sandy loam, 91 % sand and 9% clay	-
<b>AMMA Catch network Ouémé</b>	Benin	Soudanian climate with different types of rain systems and Guinean savanna vegetation.	77% sand and 19 % clay	-

438

## 439 5. Methodology of evaluation

### 440 5.1 Global comparison of SMOS and SMAP TB

441 In order to compare SMOS TB product to SMAP TB, the SMOS daily product was averaged following  
 442 the same interpolation procedure as the one suggested in the SMAP mission. The method consists in using  
 443 an inverse distance weighting for all the SMOS EASE 2.0 at 25 km grids point in the limits of the EASE  
 444 2.0 at 36 km grid of the SMAP product. The TB<sub>H</sub> and TB<sub>V</sub> from SMAP product are extracted and used as  
 445 is. The comparison is done over the pixels with a water fraction of less than 0.001 (i.e. 0.1%) since the  
 446 SMAP TBs are provided with subtracted open surface water.

447

448

## 449 5.2 Global Soil moisture maps comparison

450 Global comparison is done over the EASE-Grid 2.0 25 km used for the L3 MO SM product. The L3 MO  
451 SM field is extracted directly from the product. The L2 SO SM product is interpolated to the EASE-Grid  
452 2.0 25 km using a three stage interpolation strategy where the availability of the products inside the limits  
453 of the grid node is considered:

- 454 • bilinear, if more than two soil moisture retrievals are available.
- 455 • linear, if two soil moisture retrievals are available.
- 456 • nearest point, if one soil moisture retrieval is available.

457 The L2 SO SM is also filtered at high latitude where several soil moisture retrievals are available. The  
458 selection criterion is minimum distance from the swath centre, the same as for the L3 MO SM algorithm.

## 459 5.2 Local evaluations

460 No interpolation is used after the extraction of the SM time series. The comparison is based on the  
461 following statistical indicators:

- 462 - Mean bias ( $\text{m}^3/\text{m}^3$ )
- 463 - Standard Error of the Estimate (SEE) ( $\text{m}^3/\text{m}^3$ )
- 464 - Pearson correlation coefficient (R)
- 465 - Root mean square Error (RMSE) ( $\text{m}^3/\text{m}^3$ )

$$RMSE = \sqrt{\frac{1}{N} \sum_{i=1}^N (SM_{MO,i} - SM_{SO,i})^2} \quad (4)$$

466 Where  $SM_{MO,i}$  is the SM from multi-orbit retrievals and  $SM_{SO,i}$  is the SM from single-orbit  
467 retrievals.

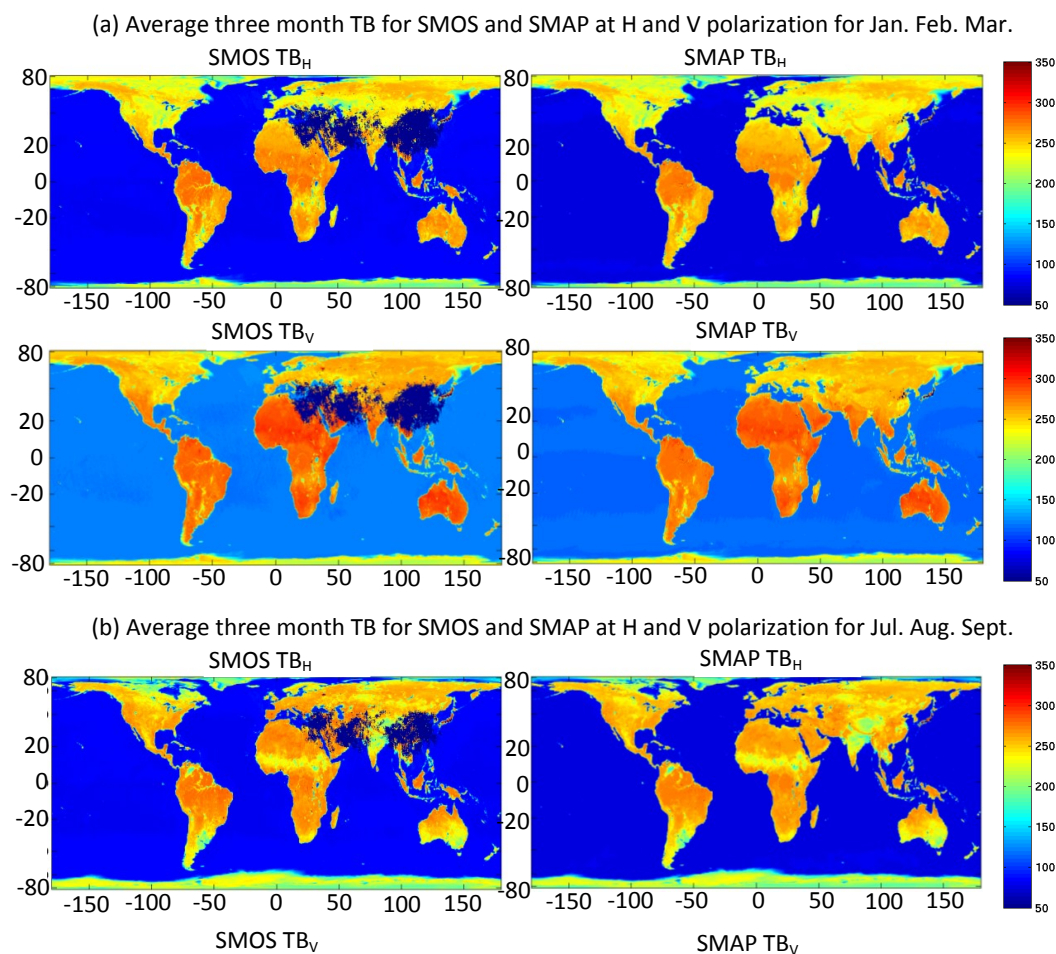
- 468 - The empirical cumulative distribution function (Cox & Oakes, 1984).

## 469 6. Results & Discussions

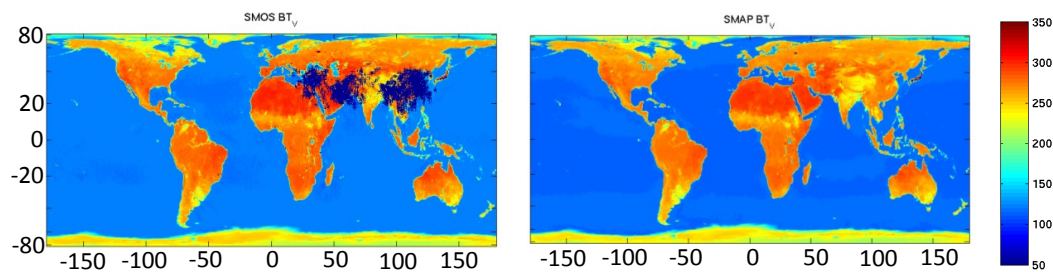
### 470 6.1 SMOS and SMAP Brightness temperatures

471 Figure 5 (a,b) and Figure 6 (a,b) show the comparison between the SMOS L3 TB and SMAP L3 TB at  $40^\circ$   
472 incidence angle. Figure 5 (a) shows the average of SMOS and SMAP  $TB_H$  and  $TB_V$  for winter (Jan., Feb.,  
473 Mar.) and summer (Jul., Aug., Sept.) seasons for year 2016. The gaps (in dark blue) in the SMOS images  
474 are due to RFI with a differentiated impact for ascending and descending orbits. The difference in TBs  
475 between H/V acquisitions is smaller than between ascending/descending configurations. The SMAP

476 products show a higher coverage because SMAP has on-board RFI filtering and mitigation which enables  
477 a better coverage but at the cost of a lower radiometric accuracy. The spatial patterns of TB are highly  
478 consistent for the two missions. Figure 6 (a,b) show the distribution of difference of  $TB_H$  and  $TB_V$  from  
479 SMOS and SMAP for winter (Jan., Feb., Mar.) and summer (Jul., Aug., Sept.) seasons during year 2016.  
480 As described in Section 5.1, only nodes with a water fraction of less than 0.01 (i.e. 1 %) are considered.  
481 The mean difference is about -3.67 K to -4.16 K with SMAP being colder independently of polarization or  
482 season. The standard deviation of all comparisons is about 3.65 K. This value is due to differences in  
483 calibration of the sensors and to the impact of differences in the acquisition time.

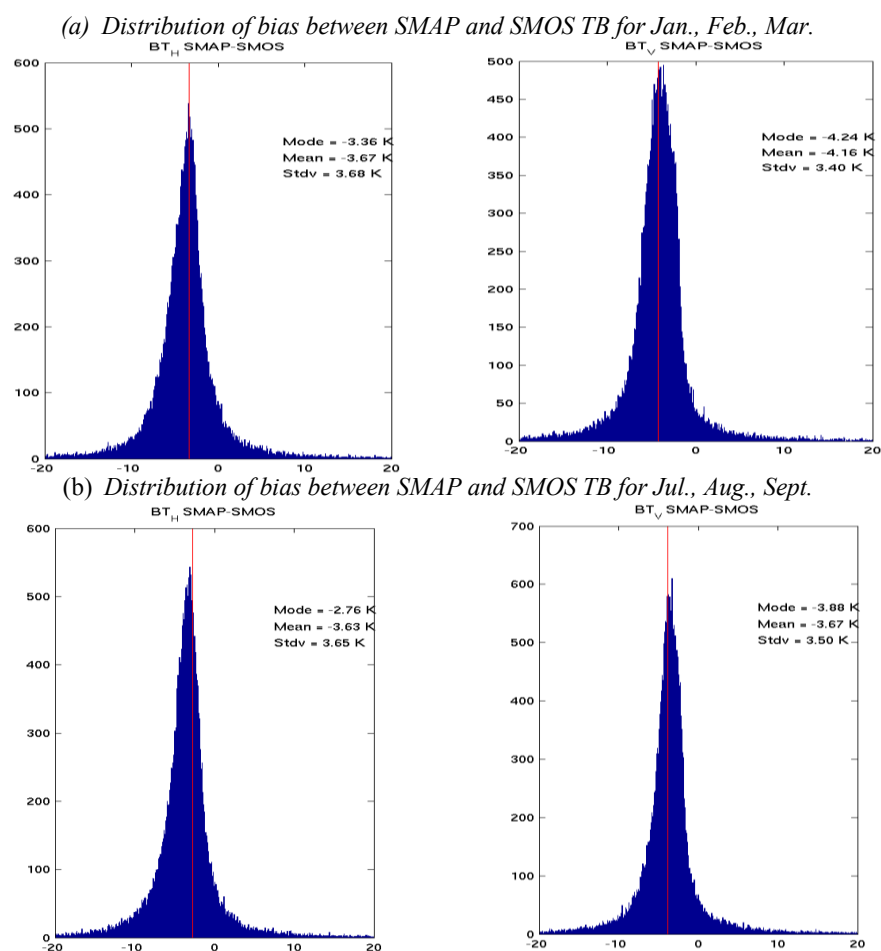






484 Figure 5 – Three month average maps of SMOS L3 TB @40° (left) and SMAP L3 TB (right) for H  
485 polarisation, V polarization considering winter: Jan., Feb., Mar. (a) and summer: Jul., Aug., Sept. (b)  
486 seasons.





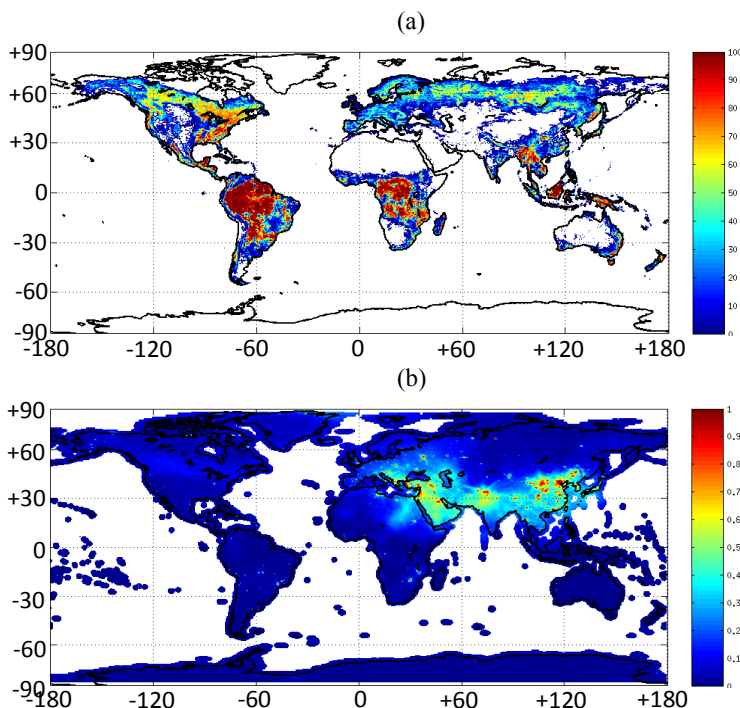
487 Figure 6 – Distribution of bias between SMAP and SMOS L3 TB for pixels with less than 1 % of water  
488 fraction for Jan. Feb. Mar. (a) and Jul. Aug. Sept. (b), H polarisation (right panel) and V polarisation  
489 (left panel).

## 490 6.2 Soil moisture retrievals at global scale

491 Based on the aforementioned evaluation methodology the L3SM MO retrievals are compared to those of  
492 L2SM SO at global scale over the 2010-2015 period. The auxiliary maps of mean forest cover percentage  
493 (Figure 8 a) and average RFI probabilities (Figure 8 b) for year 2011 are provided as complementary  
494 information. These maps are obtained from the L3SM product. The mean forest cover (Figure 8 a)  
495 provides the percentage of forest cover taking into account the mean antenna pattern. It is obtained by  
496 convoluting the ECOCLIMAP (Masson et al., 2003) forest cover by the SMOS antenna weighting  
497 function at a resolution of 4 km over an area of  $125 \times 125$  km<sup>2</sup>. The RFI map was obtained by averaging

498 the RFI probability field in the L3SM product. This information includes strong RFI and moderate RFI  
499 depicted from the SMOS full polarization brightness temperatures (Richaume et al., 2014). Some soft and  
500 mild RFI are not detected in this product.

501



502

503

504

505 *Figure 7 – Global map of the mean forest cover percentage used in the SMOS L2S0 and L3MO soil moisture*  
506 *retrievals (a) and map of the Radio Frequency interference (RFI) probabilities (b) for ascending orbit from the*  
507 *L3MO soil moisture processor.*

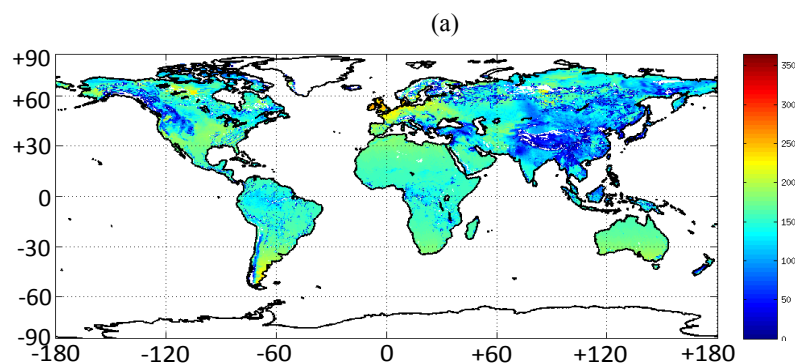
508 Figures 8 (a,b) show the mean number of successful retrievals per year (2010-2015) obtained from L3SM  
509 and L2SM respectively. White (Blank) pixels in Figure 8 (a) show the areas where no successful soil  
510 moisture retrieval is available. These pixels are mostly located in areas of dense vegetation (Congo), area  
511 that are seasonally inundated (Amazon Basin) and/or of high RFI (South-East Asia, Middle-East). From  
512 Figures 10 (a) it is clear that the coverage area of the L3SM product is higher in these areas.

513



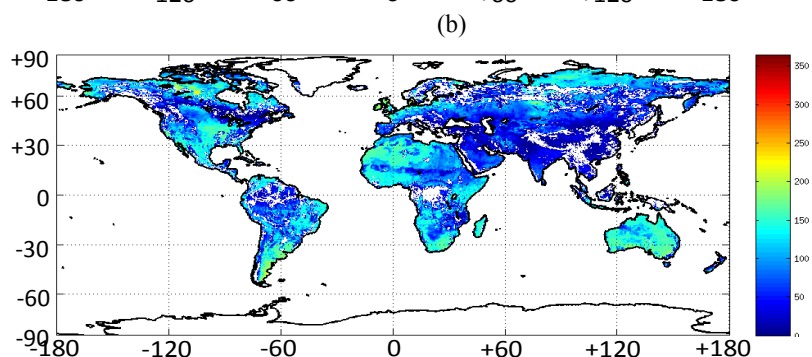
514

515



516

517



518

519 *Figure 8 – Mean number of successful SM retrievals per year (2010-2015) for ascending orbits from L3SM-MO (a),*  
520 *and L2SM-SO (b).*

521 Figures 9 (a,b) shows the difference (MO-SO) in the number of successful soil moisture retrievals  
522 between L3SM and L2SM products. The general behaviour shows a systematic increase in the number of  
523 retrievals. The number of retrievals is moderately increasing in desert and plain areas (10-20 retrievals /  
524 year / orbits). The increase is much higher for forested areas. The L2SM showed a higher number of  
525 successful retrievals in the area between 62°-70° longitude and 35°-55° latitudes. This is due to an  
526 anomaly in the processing of TB products. The ancillary data containing the Total Electronic Content  
527 (TEC) is not properly used over this region. This has been corrected and all operational products are now  
528 properly processed. The archive products will be corrected for this error in the next processing campaign.  
529 Also from Figure 13 it is clear that no enhancement in number of retrievals has been observed in areas  
530 with very high RFI probabilities in descending orbits (not shown here) like the north Asia region.

531



532

533

534

535

536

537

538

539

540

541

542

543

544

545

546

547

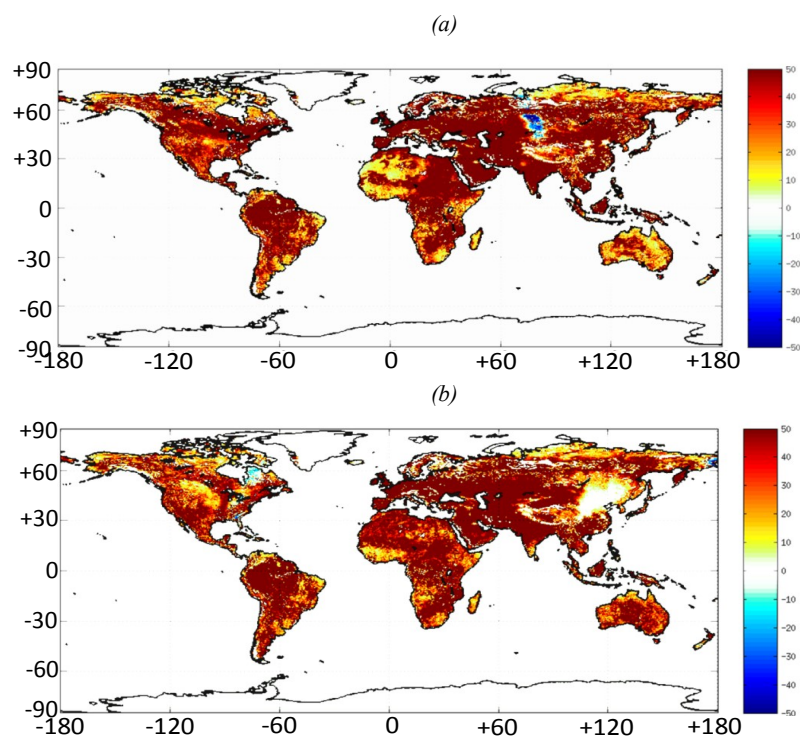
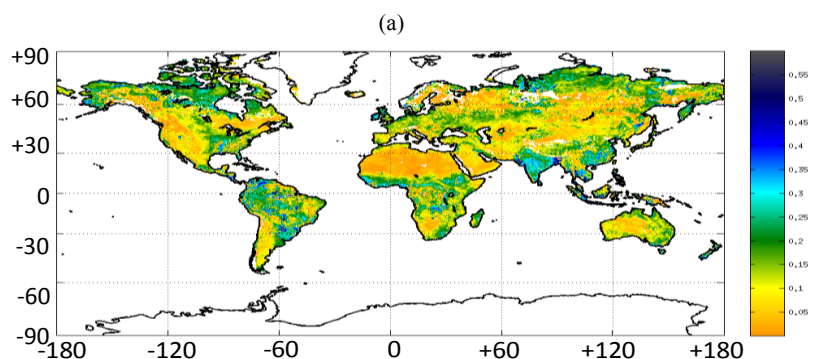


Figure 9 – Global map of the difference in the mean number of SM successful retrieval per year over 2011-2015 ( $L3SM_{MO} - L2SM_{SO}$ ) for ascending orbits (a) and descending orbits (b).

The mean soil moisture from L3SM and L2SM for ascending orbits is provided in Figures 10 (a,b). The figures show that the soil moisture spatial patterns are very similar between the SO and MO SM retrievals. The coverage of the multi-orbit product is higher as already shown in the previous figures. Nevertheless some discrepancies can be observed from the difference map (Figure 10 - c). The L3SM MO soil moisture values are generally higher than those of L2SM SO. This is most visible in forested areas (Figure 7 - a) which is consistent with climatic conditions over these areas. It is also higher in areas with high RFI pollution (Figure 7-b). This leads in general to a decrease in the value of the retrieved soil moisture values. So the higher L3SM can be due to the positive impact of using multiple dates during RFI prone periods.

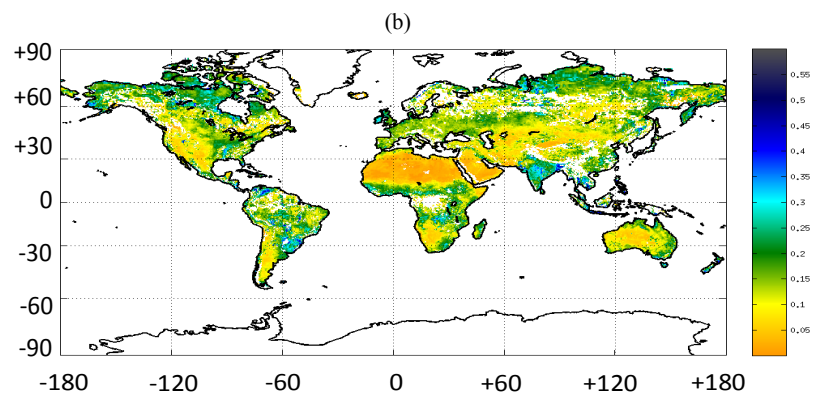
548  
549

550



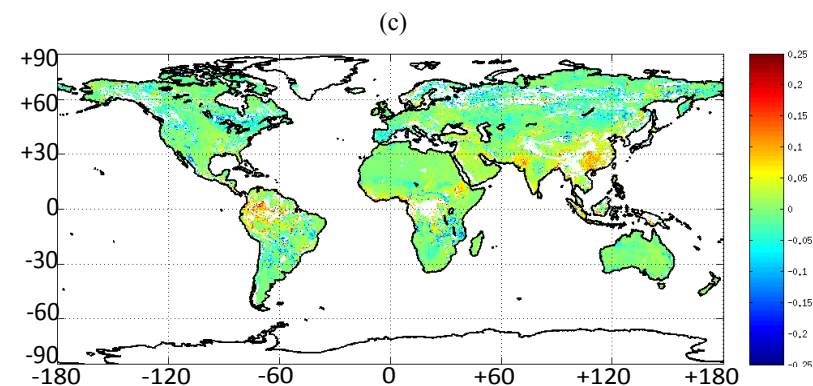
551  
552

553



554  
555

556



557  
558

559 *Figure 10 – Mean soil moisture map over 2011-2015 for ascending orbits from CATDS L3SM MO (a), DPGS L2SM*  
560 *SO (b) and the difference (MO-SO) map between L3SM<sub>MO</sub> and L2SM<sub>SO</sub> (c).*

## 561 6.2 *In situ* comparison

562 The statistics for the comparison of L2SM SO and L3SM MO with *in situ* networks is shown in Table 3  
563 and Table 4 for ascending and descending orbits respectively. The number of retrievals is systematically  
564 better for the L3SM than L2SM as expected from the global analysis. Note that, contrary to the global



565 analysis, the *in situ* analysis is done without any grid interpolation by considering the closest node. The  
 566 skills are of similar magnitude for the LW and Niger sites and the lowest skill is obtained for the Benin  
 567 site in descending overpasses. No site showed lower number of successful retrievals for L3SM than The  
 568 bias values are not much improved by the L3SM. On the contrary they seem to increase in the majority of  
 569 the sites. The correlation values range from 0.65 to 0.88 for the different sites. Increased correlation was  
 570 found for the L3SM products over the Niger site and slightly over WG in descending overpasses. The  
 571 majority of the correlation values remain high with L3SM retrieval with no significant difference between  
 572 L2SM and L3SM.

573 Table 6 – Statistics of the *in situ* vs SMOS L3SM and L2SM for ascending orbits

Site	R		Bias ( $m^3/m^3$ )		SEE ( $m^3/m^3$ )		RMSE ( $m^3/m^3$ )		Nb pt	
	L2	L3	L2	L3	L2	L3	L2	L3	L2	L3
<b>AMMA CATCH</b>										
<b>Benin</b>	0.84	0.74	-0.039	-0.058	0.056	0.082	0.068	0.101	484	552
<b>Niger</b>	0.82	0.81	-0.006	-0.003	0.052	0.047	0.052	0.047	617	644
<b>WATERSHEDS</b>										
<b>Little Washita</b>	0.83	0.82	-0.021	-0.03	0.041	0.045	0.046	0.054	625	636
<b>Walnut Gulch</b>	0.81	0.73	0.005	-0.007	0.038	0.053	0.039	0.053	638	643

Table 7 – Statistics of the *in situ* vs SMOS L3SM and L2SM for descending orbits

Site	R		Bias ( $m^3/m^3$ )		SEE ( $m^3/m^3$ )		RMSE ( $m^3/m^3$ )		Nb pt	
	L2	L3	L2	L3	L2	L3	L2	L3	L2	L3
<b>AMMA CATCH</b>										
<b>Benin</b>	0.74	0.61	-0.029	-0.037	0.069	0.104	0.075	0.11	636	667
<b>Niger</b>	0.63	0.65	-0.011	-0.008	0.049	0.049	0.05	0.05	540	598
<b>WATERSHEDS</b>										
<b>Little Washita</b>	0.81	0.80	-0.001	-0.012	0.042	0.043	0.042	0.044	333	364
<b>Walnut Gulch</b>	0.69	0.72	-0.019	-0.029	0.047	0.048	0.051	0.056	327	360

574 More in-depth analysis can be obtained by inspecting the times series of soil moisture. Figures 11 and 12  
 575 show the time series for the selected sites for the period 2010 to 2016 and for ascending and descending  
 576 overpasses. The Niger and Benin sites present a very pronounced seasonal signal typical of the Sahelian



577 sites. Over these sites the L3SM shows consistently lower soil moisture than L2SM for high soil moisture  
578 values. The L3SM is closer in this case to the site data. The time series for LW show that the SMOS data  
579 closely follows the behaviour of the soil moisture dynamics over this site. One of the reasons is that the  
580 rainfall events are well separated enabling the remote sensing data to capture the dynamics of physical  
581 processes like infiltration and evaporation at coarse scale. Thus the exponential behaviour typical of a  
582 drying soil is well depicted.

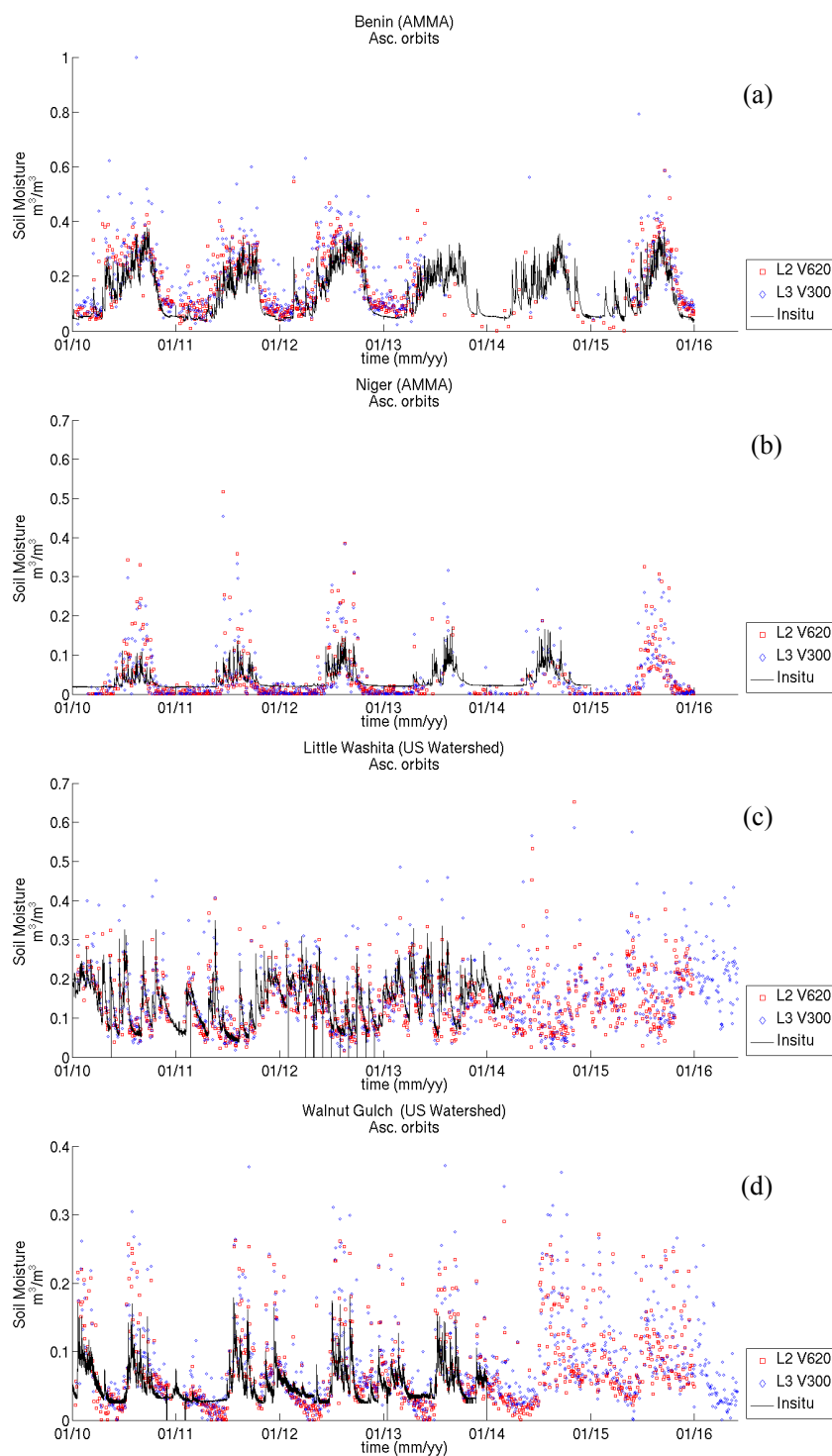


Figure 11 – Time series for the validation sites for ascending overpasses.

583  
584

585



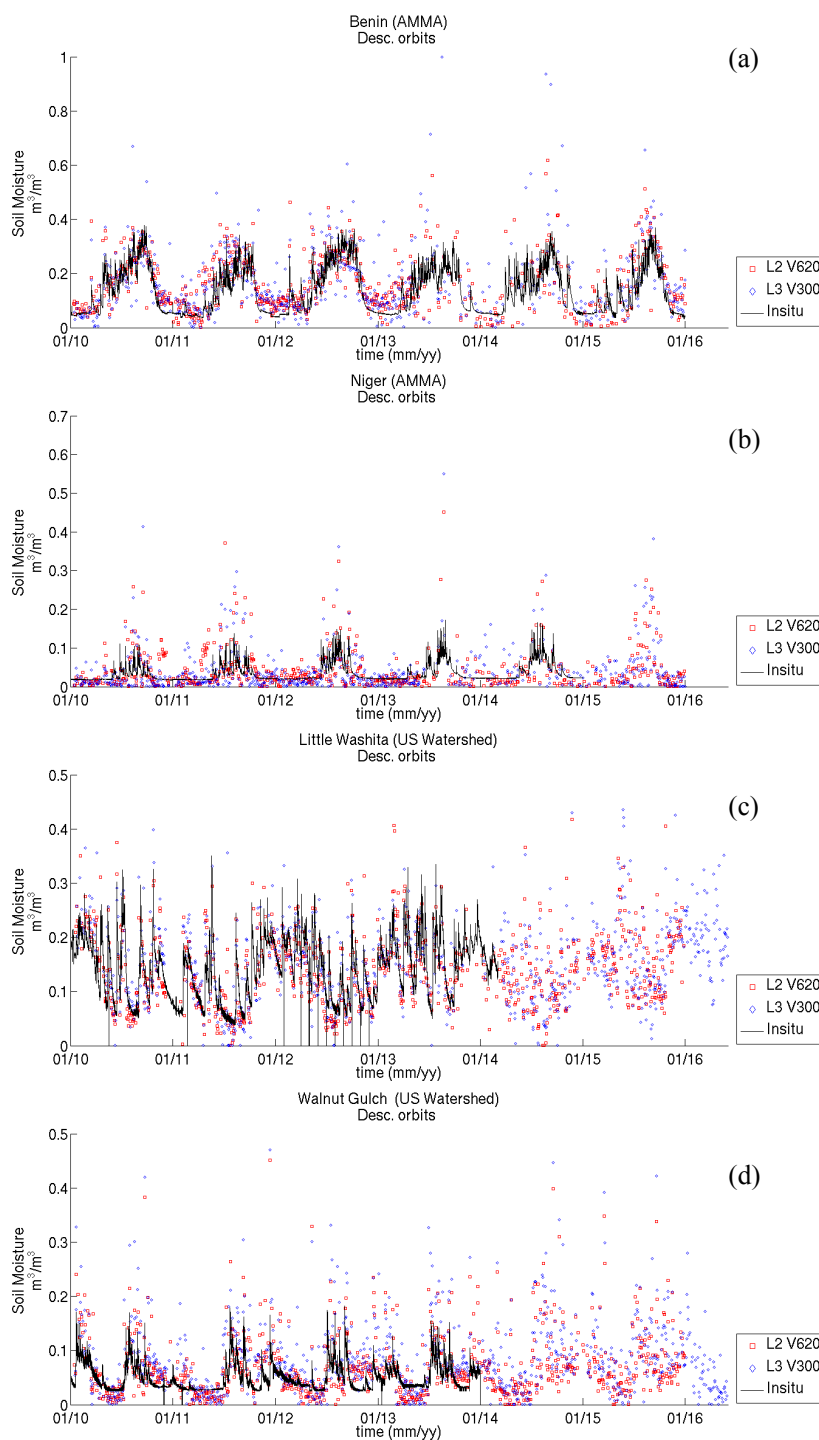
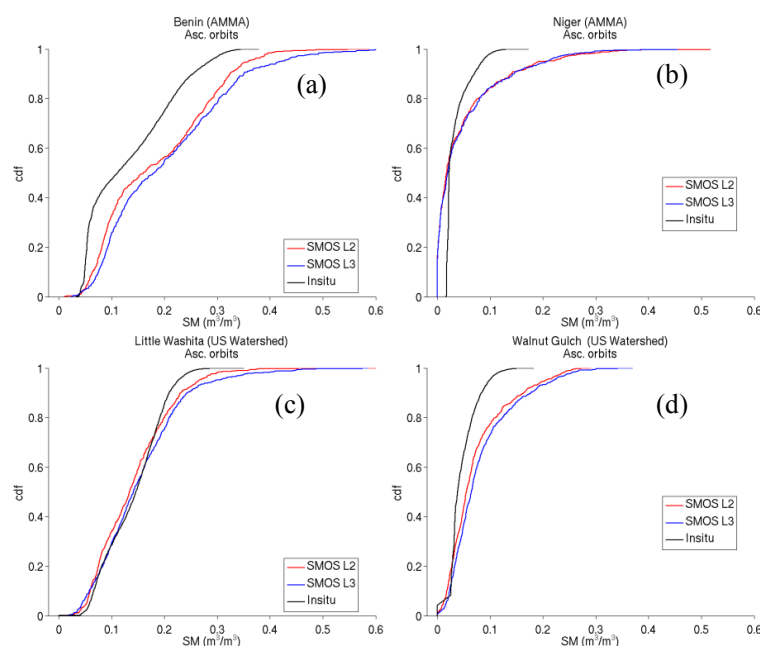


Figure 12 - Time series for the validation sites for descending overpasses.

586  
587

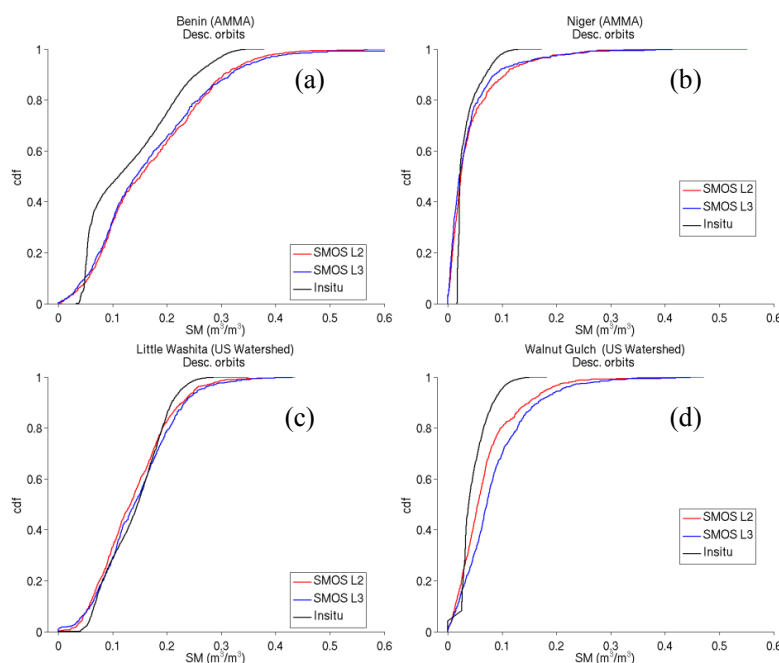
588

589  
590 Figure 13 and 14 show the CDF of the *in situ*, L2SM and L3SM data for ascending and descending orbits.  
591 From these figures it can be concluded that the SMOS soil moisture is drier than the 5 cm *in situ* data  
592 across the different values of soil moisture, this can be explained by the SMOS penetration depth with  
593 respect to that of ground sensors. Nevertheless the shape of the distribution function, describing the  
594 extreme and seasonal cycles, is well captured in most of cases. The Niger site Sahelian climate is well  
595 captured with a high probability of low soil moisture values and low number of extreme values. The  
596 differences between the L2SM and the L3SM data are mainly observed for the Benin and LW sites. When  
597 comparing figure 13 and figure 14 low differences can be notes between ascending and descending orbits.



598  
599

Figure 13 – Cumulative Distribution Function (CDF) for the validation sites for ascending overpasses.



600  
601  
602

Figure 14 - Cumulative Distribution Function (CDF) for the validation sites for descending overpasses.

## 603 7. Conclusions

604 The level 3 daily maps of soil moisture and brightness temperatures are presented in this paper. A multi-  
605 orbit soil moisture retrieval algorithm for SMOS data is used to obtain the soil moisture product. The main  
606 feature of the algorithm is the use of multiple revisits and of auto-correlation of optical vegetation depth in  
607 the cost function. The algorithm is implemented operationally at CATDS. The processing chain delivers  
608 gridded products over the EASE 2.0 grid at 25 km in NetCDF format. The L3 angle binned TB product is  
609 compared to SMAP brightness temperature maps at 40°. The results show small differences in mean TB  
610 between the products for H/V polarization and ascending and descending orbits. The SMAP product  
611 presents a wider coverage due to the on-board RFI filtering. The L3 SM product is compared to the L2  
612 SM product. The best improvements in algorithm performances are in terms of the number of successful  
613 retrievals observed over forested and RFI prone areas. Also the L3SM product shows on average wetter  
614 soil moisture retrievals than L2SM. The comparison with local sites showed that the quality of the  
615 retrieval is comparable between L2SM and L3SM. This shows that the increase in the number of  
616 successful retrieval does not degrade quality, but rather comes at the expense of an increased time lag in



617 product availability (6 hours for L2SM SO versus 3.5 to 7 days for L3SM MO ). Future works will  
618 concentrate on the associated optical thickness product not presented in this paper. An application of the  
619 algorithm to the SMAP data has been envisioned.

620

### 621 **Acknowledgements**

622 The SMOS L3SM products were obtained from the Centre Aval de Traitement des Données SMOS  
623 (CATDS), operated for the "Centre National d'Etudes Spatiales" (CNES, France) by IFREMER (Brest,  
624 France). This study was supported by the CNES "Terre, Océan, Surfaces Continentales, Atmosphère"  
625 program. The authors would like to thank the USDA-ARS Hydrology and Remote Sensing Laboratory,  
626 AMMA-Catch project for the *in situ* datasets.

### 627 **References**

- 628 Al Bitar, A., Leroux, D. J., Kerr, Y. H., Merlin, O., Richaume, P., Sahoo, A., & Wood, E. F. (2012).  
629 Evaluation of SMOS Soil Moisture Products Over Continental U.S. Using the SCAN / SNOTEL  
630 Network. *IEEE Transactions on Geoscience and Remote Sensing*, 50(5), 1572–1586.
- 631 Al-Yaari, A., Wigneron, J.P., Ducharne, A., Kerr, Y., de Rosnay, P., de Jeu, R., Govind, A., Al Bitar, A.,  
632 Albergel, C., Muñoz-Sabater, J., Richaume, P. & Mialon, A. (2014a). Global-scale evaluation of two  
633 satellite-based passive microwave soil moisture datasets (SMOS and AMSR-E) with respect to Land  
634 Data Assimilation System estimates. *Remote Sensing of Environment*, 149, 181-195
- 635 Al-Yaari, A., Wigneron, J.P., Ducharne, A., Kerr, Y.H., Wagner, W., De Lannoy, G., Reichle, R., Al  
636 Bitar, A., Dorigo, W., Richaume, P. & Mialon, A. (2014b). Global-scale comparison of passive  
637 (SMOS) and active (ASCAT) satellite based microwave soil moisture retrievals with soil moisture  
638 simulations (MERRA-Land). *Remote Sensing of Environment*, 152, 614-626
- 639 AMMA-CATCH (1996): Rivers flow and water electrical conductivity, Oueme meso site, Benin. IRD -  
640 CNRS - OSUG - OMP - OREME. doi:10.5072/AMMA-CATCH.CL.Run\_O
- 641 AMMA-CATCH (2005): Surface energy, water vapor, and carbon fluxes, Wankama local site, Niger. IRD  
642 - CNRS - OSUG - OMP - OREME. doi:10.5072/AMMA-CATCH.AE.H2OFlux\_Ncw
- 643 Brocca, L., Melone, F., Moramarco, T., Wagner, W., Naeimi, V., Bartalis, Z., & Hasenauer, S. (2010).  
644 Improving runoff prediction through the assimilation of the ASCAT soil moisture product.  
645 *Hydrology and Earth System Sciences*, 14(10), 1881-1893.
- 646 Brodzik, M. J. and K. W. Knowles. 2002. EASE-Grid: A Versatile Set of Equal-Area Projections and  
647 Grids in M. Goodchild (Ed.) *Discrete Global Grids*. Santa Barbara, California USA: National Center  
648 for Geographic Information & Analysis.



- 649 Cappelaere, B., Descroix, L., Lebel, T., Boulain, N., Ramier, D., Laurent, J.-P., Favreau, G., Boubkraoui,  
650 S., Boucher, M., Moussa, I. B., Chaffard, V., Hiernaux, P., Issoufou, H. B. A., Le Breton, E.,  
651 Mamadou, I., Nazoumou, Y., Oï, M., Ottlé, C. & Quantin, G. (2009) The AMMA-CATCH  
652 experiment in the cultivated Sahelian area of south-west Niger - Investigating water cycle response  
653 to a fluctuating climate and changing environment. *Journal of Hydrology*, 375, 34–51.
- 654 Carr D. B., Kahn, R., Sahr, K. & Olsen, T. (1997). ISEA discrete global grids *Statist. Comput. Statist.*  
655 *Graph. Newslett.*, vol. 8, no. 2/3, pp. 31–39.
- 656 Cox, D. R., & Oakes, D. (1984). *Analysis of Survival Data*. London: Chapman & Hall.
- 657 de Rosnay, P., Gruhier, C., Timouk, F., Baup, F., Mougine, E., Hiernaux, P., Kergoat, L., LeDantec, V.  
658 (2009). Multiscale soil moisture measurements at the Gourma meso-scale site in Mali. *Journal of*  
659 *Hydrology*, 375, 241–252.
- 660 de Rosnay, P., Drusch, M., Vasiljevic, D., Balsamo, G., Albergel, C., & Isaksen, L. (2013). A simplified  
661 Extended Kalman Filter for the global operational soil moisture analysis at ECMWF. *Quarterly*  
662 *Journal of the Royal Meteorological Society*, 139(674), 1199–1213.
- 663 Drusch, M. (2007). Initializing numerical weather prediction models with satellite-derived surface soil  
664 moisture: Data assimilation experiments with ECMWF's integrated forecast system and the TMI soil  
665 moisture data set. *Journal of Geophysical Research: Atmospheres*, 112(3).  
666 <http://doi.org/10.1029/2006JD007478>.
- 667 Elliott, R.L., F.R. Schiebe, K.C. Crawford, K.D. Peter and W.E. Puckett. (1993). A Unique Data  
668 Capability for Natural Resources Studies. Paper No. 932529, International Winter Meeting;  
669 American Society of Agricultural Engineers, Chicago, IL, Dec. 14-17.
- 670 Entekhabi, D., Njoku, E. G., O'Neill, P. E., Kellogg, K. H., Crow, W. T., Edelstein, W. N., Entin,  
671 J. K., Goodman, S. D., Jackson, T. J., Johnson, J., Kimball, J., Piepmeier, J. R., Koster, R.  
672 D., Martin, N., McDonald, K. C., Moghaddam, M., Moran, S., Reichle, R., Shi, J. C.,  
673 Spencer, M. W., Thurman, S. W., Tsang, L. & Zyl, J. V. (2010). The Soil Moisture Active  
674 Passive (SMAP) Mission, *Proceedings of the IEEE*, vol. 98, pp704-716.
- 675 Escorihuela, M.J., Chanzy, A., Wigneron, J.P., & Kerr, Y.H. (2010). Effective soil moisture sampling  
676 depth of L-band radiometry: A case study. *Remote Sensing of Environment*, 114, 995–1001.
- 677 Guérif, M., & Duke, C. (2000). Adjustment procedures of a crop model to the site specific characteristics  
678 of soil and crop using remote sensing data assimilation. *Agriculture, Ecosystems & Environment*.  
679 [http://doi.org/10.1016/S0167-8809\(00\)00168-7](http://doi.org/10.1016/S0167-8809(00)00168-7)
- 680 Hagolle, O., Dedieu, G., Mougine, B., Debaecker, V., Duchemin, B., & Meygret, A. (2008). Correction  
681 of aerosol effects on multi-temporal images acquired with constant viewing angles: Application to  
682 Formosat-2 images. *Remote Sensing of Environment*, 112(4), 1689–1701.
- 683 Hagolle, O., Huc, M., Pascual, D. V., & Dedieu, G. (2010). A multi-temporal method for cloud detection,  
684 applied to FORMOSAT-2, VEN $\mu$ S, LANDSAT and SENTINEL-2 images. *Remote Sensing of*  
685 *Environment*, 114(8), 1747–1755.
- 686 Hagolle, O., Huc, M., Villa Pascual, D., & Dedieu, G. (2015). A Multi-Temporal and Multi-Spectral  
687 Method to Estimate Aerosol Optical Thickness over Land, for the Atmospheric Correction of  
688 FormoSat-2, LandSat, VEN $\mu$ S and Sentinel-2 Images. *Remote Sensing*, 7(3), 2668–2691.



- 689 Hollmann, R., Merchant, C. J., Saunders, R., Downy, C., Buchwitz, M., Cazenave, A., ... & Wagner, W.  
690 (2013). The ESA climate change initiative: Satellite data records for essential climate  
691 variables. *Bulletin of the American Meteorological Society*, 94(10), 1541-1552.
- 692 Inglada, J., & Mercier, G. (2007). A new statistical similarity measure for change detection in  
693 multitemporal SAR images and its extension to multiscale change analysis. *Geoscience and Remote  
694 Sensing, IEEE Transactions on*, 45(5), 1432-1445.
- 695 Jackson, T. J., & Schmugge, T. J. (1991). Vegetation effects on the microwave emission of soils, *Remote  
696 Sensing of Environment*, 36(3), 203-212.
- 697 Jackson T. J., M. H. Cosh, R. Bindlish, P. J. Starks, D. D. Bosch, M. Seyfried, D. C. Goodrich, M. S.  
698 Moran, and J. Du. (2010). Validation of Advanced Microwave Scanning Radiometer soil moisture  
699 products. *IEEE Trans. Geosci. Remote Sens.*, vol. 48, no. 12, pp. 4256–4272, Dec. 2010.
- 700 Jackson T. J., Bindlish R., Cosh M., Zhao T., Starks P., Bosch D., Seyfried M., Moran M. S., Goodrich  
701 D., Kerr Y. H., and Leroux D. (2012). Validation of Soil Moisture and Ocean Salinity (SMOS) Soil  
702 Moisture Over Watershed Networks in the U.S.", *IEEE Trans. Geosci. Remote Sens*, VOL. 50, NO.  
703 5.
- 704 Jung, M., Reichstein, M., Ciais, P., Seneviratne, S. I., Sheffield, J., Goulden, M. L., ... & Dolman, A. J.  
705 (2010). Recent decline in the global land evapotranspiration trend due to limited moisture  
706 supply. *Nature*, 467(7318), 951-954.
- 707 Keefer, T. O., M. S. Moran, and G. B. Paige (2008), Long-term meteorological and soil hydrology  
708 database, Walnut Gulch Experimental Watershed, Arizona, United States, *Water Resour. Res.*, 44,  
709 W05S07, doi:10.1029/2006WR005702.
- 710 Kerr, Y. H., & Njoku, E. G. (1990). Semiempirical model for interpreting microwave emission from  
711 semiarid land surfaces as seen from space. *IEEE Transactions on Geoscience and Remote Sensing*,  
712 28(3), 384–393. <http://doi.org/10.1109/36.54364>
- 713 Kerr, Y. H., Waldteufel, P., Wigneron, J.-P., Martinuzzi, J. M., Font, J., & Berger, M. (2001). Soil  
714 moisture retrieval from space: The Soil Moisture and Ocean Salinity (SMOS) mission. *IEEE  
715 Transactions on Geoscience and Remote Sensing*, 39(8), 1729–1735.  
716 <http://doi.org/10.1109/36.942551>
- 717 Kerr, Y. H., Waldteufel, P., Wigneron, J.-P., Delwart, S., Cabot, F., Boutin, J., ... Mecklenburg, S. (2010).  
718 The SMOS Mission: New Tool for Monitoring Key Elements of the Global Water Cycle.  
719 *Proceedings of the IEEE*, 98(5), 666–687. <http://doi.org/10.1109/JPROC.2010.2043032>
- 720 Kerr, Y. H., Waldteufel, P., Richaume, P., Wigneron, J.-P., Ferrazzoli, P., Mahmoodi, A., Al Bitar, A.,  
721 Cabot, F., Gruhier, C., Enache Juglea, S., Leroux, D., Mialon, A. and Delwart, S. (2012). The  
722 SMOS Soil Moisture Retrieval Algorithm. *Geoscience and Remote Sensing*, 50(5), 1384–1403.
- 723 Kerr, Y. H., Jacqueline, E., Al Bitar, A., Cabot, F., Mialon, A., & Richaume, P. (2013). CATDS SMOS L3  
724 soil moisture retrieval processor, Algorithm Theoretical Baseline Document (ATBD).
- 725 Keyantash, J., & Dracup, J. A. (2002). The quantification of drought: an evaluation of drought indices.  
726 *Bulletin of the American Meteorological Society*, 83(8), 1167-1180.



- 727 Khazâal A., Anterrieu, E., Cabot, F., Kerr, Y. H. (2016). Impact of Direct Solar Radiations Seen by the  
728 Back-Lobes Antenna Patterns of SMOS on the Retrieved Images. *IEEE Journal of Selected Topics*  
729 *in Applied Earth Observations and Remote Sensing*, vol.PP, no.99, pp.1-8.
- 730 Konings, A. G., Piles, M., Rötzer, K., McColl, K. A., Chan, S. K., & Entekhabi, D. (2016). Vegetation  
731 optical depth and scattering albedo retrieval using time series of dual-polarized L-band radiometer  
732 observations. *Remote sensing of environment*, 172, 178-189.
- 733 Koster, R. D., Dirmeyer, P. A., Guo, Z., Bonan, G., Chan, E., Cox, P., ... & Yamada, T. (2004). Regions  
734 of strong coupling between soil moisture and precipitation. *Science*, 305(5687), 1138-1140.
- 735 Rodgers L., & Nicewander A., (1988). Thirteen ways to look at the correlation coefficient. *The American*  
736 *Statistician*, 42(1), 59–66.
- 737 Lievens, H., Tomer, S. K., Al Bitar, A., De Lannoy, G. J. M., Drusch, M., Dumedah, G., Franssen, H.J.H.,  
738 Kerr, Y. H., Martens, B., Pan, M. and Roundy, J. K. (2015). SMOS soil moisture assimilation for  
739 improved hydrologic simulation in the Murray Darling Basin, Australia. *Remote Sensing of*  
740 *Environment*, 168, pp.146-162.
- 741 Leroux D. J., Kerr Y. H., Al Bitar A., Bindlish R., Jackson T., Berthelot B., and Portet G. (2014).  
742 Comparison Between SMOS, VUA, ASCAT, and ECMWF Soil Moisture Products Over Four  
743 Watersheds in U.S., *IEEE Transactions on Geoscience and Remote Sensing*, VOL. 52, 3.
- 744 Liu, S. F., Liou, Y.-A., Wang, W. J., Wigneron, J. -P., & Lee, J. B. (2002). Retrieval of crop biomass and  
745 soil moisture from measured 1.4 and 10.65 brightness temperatures. *IEEE Transactions on*  
746 *Geoscience and Remote Sensing*, 40(6), 1260–1268
- 747 Louvet S., Pellarin T., Al Bitar A., Cappelaere B. Galle Sylvie, Grippa M., Gruhier C., Kerr Y., Lebel T.,  
748 Mialon A., Mougin E., Quantin G., Richaume P., & de Rosnay P. (2015) SMOS soil moisture  
749 product evaluation over West-Africa from local to regional scale, *Remote Sensing of Environment*,  
750 Volume 156, January 2015, Pages 383-394, ISSN 0034-4257,  
751 <http://dx.doi.org/10.1016/j.rse.2014.10.005>.
- 752 Masson V., Champeaux J.-L., Chauvin F., Meriguet C., & Lacaze R. (2003) A Global Database of Land  
753 Surface Parameters at 1-km Resolution in Meteorological and Climate Models, *J. Clim.*, 16,1261-  
754 1282, 2003.
- 755 Mattia, F., Satalino, G., Pauwels, V. R. N., & Loew, A. (2009). Soil moisture retrieval through a merging  
756 of multi-temporal L-band SAR data and hydrologic modelling. *Hydrology and Earth System*  
757 *Sciences*, 13(3), 343-356.
- 758 Mialon, A., Richaume, P., Leroux, D., Bircher, S., Al Bitar, A., Pellarin, T., ... & Kerr, Y. H. (2015).  
759 Comparison of Dobson and Mironov dielectric models in the SMOS soil moisture retrieval  
760 algorithm. *IEEE Transactions on Geoscience and Remote Sensing*, 53(6), 3084-3094.
- 761 Miernecki, M., Wigneron, J. P., Lopez-Baeza, E., Kerr, Y., De Jeu, R., De Lannoy, G. J., ... & Richaume,  
762 P. (2014). Comparison of SMOS and SMAP soil moisture retrieval approaches using tower-based  
763 radiometer data over a vineyard field. *Remote Sensing of Environment*, 154, 89-101.
- 764 Mo, T., Choudhury, B. J., Schmugge, T. J., Wang, J. R., & Jackson, T. J. (1982). A model for microwave  
765 emission from vegetation-covered fields. *Journal of Geophysical Research*, 87, 11.229–11.237.





- 766 Mougín, E., Hiernaux, P., Kergoat, L., Grippa, M., de Rosnay, P., Timouk, F., et al. (2009). The AMMA-  
767 CATCH Gourma observatory site in Mali: Relating climatic variations to changes in vegetation,  
768 surface hydrology, fluxes and natural resources. *Journal of Hydrology*, 375, 14–33.
- 769 Naeimi, V., Scipal, K., Bartalis, Z., Hasenauer, S., & Wagner, W. (2009). An improved soil moisture  
770 retrieval algorithm for ERS and METOP scatterometer observations. *IEEE Transactions on*  
771 *Geoscience and Remote Sensing*, 47(7), 1999-2013.
- 772 Njoku, E. G., & Entekhabi, D. (1996). Passive microwave remote sensing of soil moisture. *Journal of*  
773 *Hydrology*. [http://doi.org/10.1016/0022-1694\(95\)02970-2](http://doi.org/10.1016/0022-1694(95)02970-2)
- 774 Njoku, E. G., Jackson, T. J., Lakshmi, V., Chan, T. K., & Nghiem, S. V. (2003). Soil moisture retrieval  
775 from AMSR-E. *IEEE Transactions on Geoscience and Remote Sensing*, 41(2), 215-229.
- 776 O'Neill, P., Chan, S., Njoku, E., Jackson, T., & Bindlish, R. (2012). Soil Moisture Active Passive (SMAP)  
777 Algorithm Theoretical Basis Document (ATBD). SMAP Level 2 & 3 Soil Moisture (Passive),  
778 (L2\_SM\_P, L3\_SM\_P). Initial Release, 1,  
779 ([http://smap.jpl.nasa.gov/files/smap2/L2&3\\_SM\\_P\\_InitRel\\_v1\\_filt2.pdf](http://smap.jpl.nasa.gov/files/smap2/L2&3_SM_P_InitRel_v1_filt2.pdf)).
- 780 Oliva, R., Daganzo-Eusebio, E., Kerr, Y. H., Mecklenburg, S., Nieto, S., Richaume, P., & Gruhier, C.  
781 (2012). SMOS radio frequency interference scenario: Status and actions taken to improve the RFI  
782 environment in the 1400-1427-MHZ passive band. *IEEE Transactions on Geoscience and Remote*  
783 *Sensing*, 50(5 PART 1), 1427–1439. <http://doi.org/10.1109/TGRS.2012.2182775>
- 784 Owe, M., de Jeu, R., & Holmes, T. (2008). Multisensor historical climatology of satellite-derived global  
785 land surface moisture. *Journal of Geophysical Research: Earth Surface*, 113(F1).
- 786 Pellarin, T., Laurent, J.P., Cappelaere, B., Decharme, B., Descroix, L., & Ramier, D. (2009). Hydrological  
787 modelling and associated microwave emission of a semi-arid region in South-western Niger. *Journal*  
788 *of Hydrology*, 375, 262–272.
- 789 Rahmoune, R., Ferrazzoli, P., Singh, Y. K., Kerr, Y. H., Richaume, P., & Al Bitar, A. (2014). SMOS  
790 Retrieval Results Over Forests: Comparisons With Independent Measurements. *Selected Topics in*  
791 *Applied Earth Observations and Remote Sensing*, *IEEE Journal of*, 7(9), 3858-3866.
- 792 Richaume, P., Soldo, Y., Anterrieu, E., Khazaal, A., Bircher, S., Mialon, A., Al Bitar, A., Rodriguez-  
793 Fernandez, N., Cabot, F., Kerr, Y., Mahmoodi, A., "RFI in SMOS measurements: Update on  
794 detection, localization, mitigation techniques and preliminary quantified impacts on soil moisture  
795 products," *Geoscience and Remote Sensing Symposium (IGARSS)*, 2014 IEEE International , vol.,  
796 no.,pp.223,226, 13-18 July 2014 doi: 10.1109/IGARSS.2014.6946397
- 797 Rodríguez-Fernández, N. J., Aires, F., Richaume, P., Kerr, Y. H., Prigent, C., Kolassa, J., Cabot, F.,  
798 Mahmoodi, A., Jimenez, J. C. & Drusch, M. (2015). Soil moisture retrieval using neural networks:  
799 application to SMOS. *IEEE Transactions on Geoscience and Remote Sensing*, 53(11), 5991-6007.
- 800 Sahoo A. K., P. R. Houser, C. Ferguson, E. F. Wood, P. A. Dirmeyer, and M. Kafatos, "Evaluation of  
801 AMSR-E soil moisture results using the insitu data over the Little River Experimental Watershed,  
802 Georgia," *Remote Sens. Environ.*, vol. 112, no. 6, pp. 3142–3152, Jun. 2008.
- 803 Saleh, K., Wigneron, J. -P., De Rosnay, P., Calvet, J. -C., & Kerr, Y. (2006). Semi-empirical regressions at  
804 L-band applied to surface soil moisture retrievals over grass. *Remote Sensing of Environment*, 101,  
805 415–426.





- 806 Tomer, S. K., Al Bitar, A., Sekhar, M., Zribi, M., Bandyopadhyay, S., Sreelash, K., ... & Kerr, Y. (2015).  
807 Retrieval and Multi-scale Validation of Soil Moisture from Multi-temporal SAR Data in a Semi-Arid  
808 Tropical Region. *Remote Sensing*, 7(6), 8128-8153.
- 809 Ulaby, F. T., Dubois, P. C., & van Zyl, J. (1996). Radar mapping of surface soil moisture. *Journal of*  
810 *Hydrology*, 184(1-2), 57–84. [http://doi.org/10.1016/0022-1694\(95\)02968-0](http://doi.org/10.1016/0022-1694(95)02968-0)
- 811 Verhoest, N. E., Troch, P. A., Paniconi, C., & De Troch, F. P. (1998). Mapping basin scale variable source  
812 areas from multitemporal remotely sensed observations of soil moisture behavior. *Water Resources*  
813 *Research*, 34(12), 3235-3244.
- 814 Wagner, W., Lemoine, G. & Rott, H. (1999). A Method for Estimating Soil Moisture from ERS  
815 Scatterometer and Soil Data. *Remote Sens. Environ.* 70, 191–207.
- 816 Wagner, W., Hahn, S., Kidd, R., Melzer, T., Bartalis, Z., Hasenauer, S., Figa, J., de Rosnay, P., Jann, A.,  
817 Schneider, S., Komma, J., Kubu, G., Brugger, K., Aubrecht, C., Zuger, J., Gangkofner, U.,  
818 Kienberger, S., Brocca, L., Wang, Y., Bloeschl, G., Eitzinger, J., Steinnocher, K., Zeil, P. & Rubel,  
819 F. (2013). The ASCAT Soil Moisture Product: A Review of its Specifications, Validation Results,  
820 and Emerging Applications. *Meteorologische Zeitschrift*, 22(1), 5-33.
- 821 Wigneron, J.-P., Calvet, J.-C., de Rosnay, P., Kerr, Y., Waldteufel, P., Saleh, K., et al. (2004). Soil  
822 moisture retrievals from bi-angular L-band passivemrowave observations. *IEEE Transactions on*  
823 *Geoscience and Remote Sensing Letters*, 1(4), 277–281.
- 824 Wigneron, J.-P., Kerr, Y. H., Waldteufel, P., Saleh, K., Escorihuela, M.-J., Richaume, P., ... & Schwank,  
825 M. (2007). L-band Microwave Emission of the Biosphere (L-MEB) Model: Description and  
826 calibration against experimental data sets over crop fields. *Remote Sensing of Environment*, 107,  
827 639–655. <http://doi.org/10.1016/j.rse.2006.10.014>
- 828